Improved Ice Growth Modeling Based on Close-Up Analysis of Aircraft Ice Accretion

by

Didier Haim Hazan

BSc Cum Laude, Technion, Israel Institute of Technology (1988)

Submitted to the Department of Aeronautics and Astronautics
in partial fulfillment of the requirements for the degree of

Master of Science in Aeronautics and Astronautics

at the

MASSACHUSETTS INSTITUTE OF TECHNOLOGY

June 1993

Author .....
Department of Aeronautics and Astronautics
June 8, 1993

Certified by ....
Kenneth S. Breuer
Assistant Professor
Thesis Supervisor

Certified by .....
R. John Hansman
Associate Professor
Thesis Supervisor

Accepted by .....
Professor Harold Y. Wachman
Chairman, Department Graduate Committee

Improved Ice Growth Modeling Based on Close-Up Analysis of Aircraft Ice Accretion

by

Didier Haim Hazan

Submitted to the Department of Aeronautics and Astronautics
on June 8, 1993, in partial fulfillment of the
requirements for the degree of
Master of Science in Aeronautics and Astronautics

Abstract

Icing wind tunnel tests were conducted at the NASA Lewis Icing Research Tunnel, on small cylinders and a laminar type airfoil. The stagnation and off-stagnation regions were observed with close-up video cameras, to gain more understanding of the freezing processes occurring in aircraft ice accretion. In pure rime ice regimes feathers covered the whole impingement region. In the mixed ice regime, rime feathers covered most of the impingement region, while runback water was observed to freeze in between the feathers. In the pure glaze ice regimes, no feather formation was observed. Two types of horns were identified. Mixed horns labelled Type A horns, and glaze horns labelled Type B horns. Type A horns grew in the impingement direction close to the stagnation line, and were observed in some mixed ice regimes. Type B horns grew normal to the surface at a more downstream position, and were observed in most glaze ice regimes. The feather growth was analyzed and growth rates extracted from the video data. Since all feathers could be traced back to some initial ice roughness, dry wind tunnel tests were conducted to investigate the local heat transfer increase experienced by such roughness element on a flat plate, using infrared thermography techniques. In a turbulent boundary layer, small individual roughness experienced at their tip, a 250% increase in convective heat transfer coefficient. An improved ice growth model is proposed that includes most of the physical processes observed. Impinging and runback water are separated for the mass and energy balances. Subsequently, feather growth limits on the body are calculated. An enhanced convective heat transfer coefficient is used for the feather growth. Feathers are grown in a bulk approach, with runback water allowed to freeze in its inside by rising the ice density.

Thesis Supervisor: Kenneth S. Breuer
Title: Assistant Professor

Thesis Supervisor: R. John Hansman
Title: Associate Professor

Contents

List of Figures

List of Tables

Chapter 1

Introduction

After more than fifty years of research, icing remains a concern for aviation constructors and authorities [1, 2]. The efforts to study the phenomenon began in the early forties, and lead mainly to the implementation of ice protection devices and safety regulations. In the last decade, however, reports on numerous icing accidents have intensified research on aircraft ice accretion.

1.1 Icing in Aviation

Icing occurs when an aircraft passes through a cloud containing supercooled water droplets at a temperature below 0°C. The severity of the accretion is dependent on meteorological conditions, flight conditions, aircraft geometry, pilot performance, and ice protection system effectiveness. In order to design efficient ice protection systems, it is valuable to know where and how much ice will form. Specially equipped testplanes fly perilous and costly research missions in natural or artificial icing clouds, to observe and study ice accretion, or simply to certify an aircraft for flight in specific icing conditions. In addition to these flights, certification can be granted through the testing of vital components in icing wind tunnels, and, whenever possible, the computer simulation of ice accretion. The few existing icing wind tunnels have serious limitations due to their limited range of airspeed, ambient temperature, cloud's water content, droplet size and even their availability.

Ideally, most of the certification of an aircraft for flight in icing conditions should be achieved through accurate ice accretion computer simulation. This would reduce the cost, time and dangers of actual flight tests, and avoid the limitations of wind tunnel testing.

1.2 Icing Parameters

Different types of ice form on aircraft in flight, depending on the external conditions. The primary governing parameters are :

- The ambient air temperature.
- The aircraft's airspeed.
- The liquid water content (LWC), usually expressed in g/m^3.
- The mean volume diameter (MVD), characterizes the droplet sizes in a cloud by a single parameter.
- The geometry of the problem (e.g: aircraft shapes or angle of attack).

Any change in one of the above factors can affect the resulting ice shape and composition. In addition to the governing parameters, the following four quantities will be extensively used in the present research and need to be defined:

- The impingement limits: the furthest aft locations, on the upper (su) and lower surfaces (sl) of a body, at which the water particles impact (figure 1-1).
- The freezing fraction: the fraction of the mass of water added to a body that is able to freeze.
- The collection efficiency: the measure of objects' ability to capture incoming water droplets. It is the ratio of an upstream water flux cross-sectional area (dy_o) to the impact area on the body (ds). The local collection efficiency β can be defined as follows (figure 1-1):

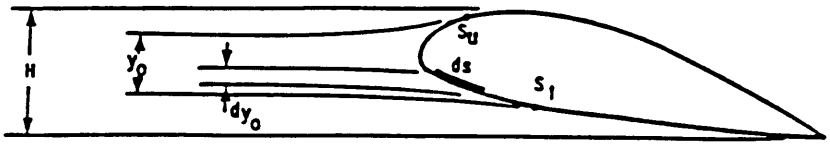

s_u = Upper – Surface Impingement Limit
s_l = Lower – Surface Impingement Limit
H = Forward Projection of the Airfoil Height

Figure 1-1: Collection efficiency and impingement limits on a body [2]

$$\beta = \frac{dy_0}{ds} \tag{1.1}$$

- The runback water: the portion of the water on a body that has not yet been frozen, and is moving along the body.

Both the freezing fraction and the collection efficiency can be defined as total values over the whole body, or as local values at a body coordinate.

1.3 Different Types of Ice Growth

Depending upon the governing parameters, three kinds of ice are commonly observed in aircraft ice accretion. Note that all three types of ice growth might be present on a single body, since local freezing fractions may vary from one body coordinate to another.

- *Rime ice*: ice formed at relatively cold temperatures and low LWC. Characterized by an opaque white or *milky* color and relatively aerodynamic shape. The rime ice is formed by droplets that freeze on impact and trap air bubbles, giving it the *milky* appearance and low density (figure 1-2). It is also referred to as *dry* growth.

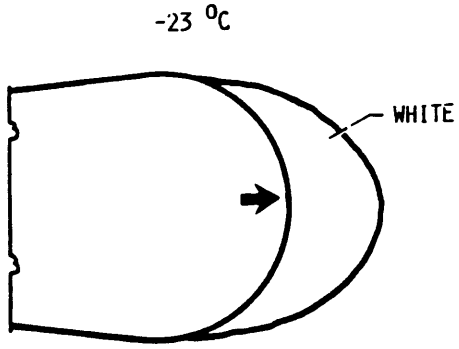

Figure 1-2: Rime ice: Airspeed: 200 mph; MVD: 30 μm; LWC: 0.5 g/m^3 [17]

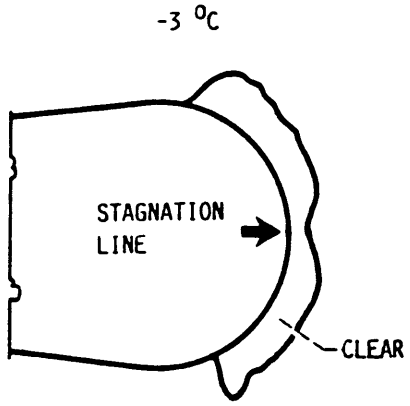

Figure 1-3: Glaze ice: Airspeed: 200 mph; MVD: 30 μm; LWC: 0.5 g/m^3 [17]

- *Glaze ice*: ice formed at relatively warmer temperatures and high LWC. Characteristically clear with unfrozen water on its surface, and possible lobes called *horns*, developing away from the stagnation region. Glaze ice is accompanied by water runback in the form of *film* or *rivulets* (figure 1-3), and is also referred to as *wet* growth.

- *Mixed ice*: as its name indicates, it presents characteristics of both rime and glaze ice. Mixed ice appears when the governing parameters are such that, locally, wet and dry ice growths may take place (figure 1-4)

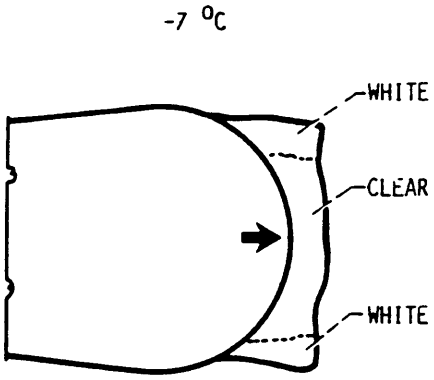

Figure 1-4: Mixed ice: Airspeed: 200 mph; MVD: 30 μm; LWC: 0.5 g/m^3 [17]

1.4 Prediction Techniques

1.4.1 Testing

The prevalent form of icing research and aircraft certification has always been through testing. Aircraft icing tests usually consist in one of the following two techniques:

1. Flight test in natural or artificial icing conditions:

   - Testing in *natural* icing conditions requires flying into icing clouds, as well as measuring the external conditions. This is a time-consuming and dangerous test that is often costly [2, 3].
   - Testing in *artificial* icing conditions. This requires the intervention of a second aircraft that will *shower* the test plane with an artificial cloud of droplets. This might be less time-consuming than the natural case, but it results in unrealistic icing conditions [2, 4].

2. Scale model or full size wind tunnel testing. Icing wind tunnels have been developed since the early forties [5]. There are again two categories:

   - Open-air icing wind tunnels: these take advantage of natural icing conditions (clouds and/or temperature) from elevated laboratories, usually on the top of a mountain (e.g. Modane, ONERA [6]).

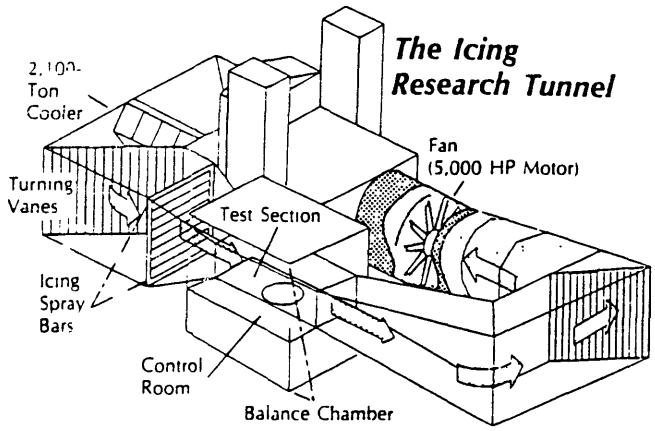

Figure 1-5: NASA Lewis Icing Research Wind Tunnel (IRT)

- Closed icing wind tunnels: which require large refrigeration facilities and a spray of supercooled water droplets. The dimensions of their test section are therefore greatly limited. The largest icing wind tunnel in the West, the NASA-Lewis Icing Research Tunnel (*IRT*) has a 6ft x 9ft test section, and has a 2100 ton air cooler (figure 1-5). The few large icing wind tunnels will allow for the testing of full size aircraft components, such as antennas, helicopter rotors, or jet intakes [5, 22].

1.4.2 Ice Accretion Prediction Codes

Numerical programs have been developed to simulate aircraft ice accretion [8]. The simulations must start by calculating the flow field around the body. The flow field data is used, thereafter, to compute the trajectory of the impinging water droplets. Then, the ice accretion prediction codes calculate the impingement limits and the local collection efficiencies. The convective heat transfer coefficients need to be evaluated on the body, using the flow field data, before calculating the local mass and energy balances, and the local freezing fractions. Once all this data is gathered, the ice accretion programs define the accretion shape and structure, and therefore, the new body shape. The common denominator of these programs is that they all consist of four distinct modules, interconnected as described in figure 1-6:

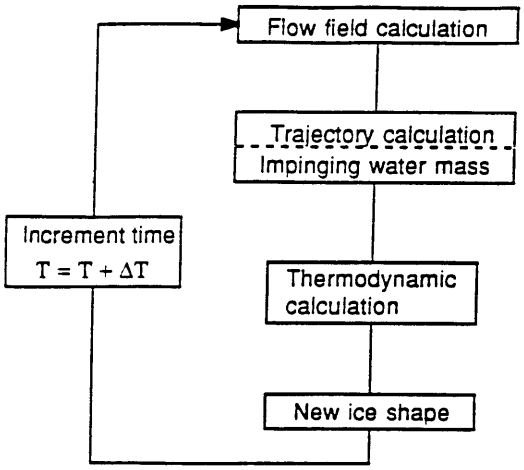

Figure 1-6: Typical modular structure of ice accretion simulation [20]

1. The flow solver: 2D and 3D codes have been written to compute the flow around bodies with the following methods:

   - Panel method: fast but does not capture separation and gives inaccurate velocity field near panels. Combined with integral boundary layer calculation.
   - Interactive boundary layer method: no separation but an efficient way to deal with viscous effects.
   - Euler/Navier-Stokes codes, with structured or unstructured grid: these codes capture separations, handle accurately viscous effects but require long computer runs and have difficulty with complex grids required for ice shapes [9].

2. The droplet trajectory module: calculates water droplets trajectories from some upstream location until they impact on the surface or fly pass the body. Determines the impingement limits on the body (2D or 3D), and the droplets impact location pattern in-between. It then calculates the local collection efficiencies on the body.

3. Mass and energy balances on each panel or grid element: most codes are based on Messinger's thermodynamic model [10] of ice growth process. This module

would usually include the calculation of the heat transfer coefficient.

4. Ice growth model: the local freezing fractions are known and ice is grown on the element with the calculated ice density and height, creating the new body.

This is the sequence of calculation for each time-step of a typical ice accretion prediction code. In the scope of this work, Lewice, NASA Lewis' ice accretion prediction code, will be the basis for discussion. Lewice embodies a 2D panel code to calculate the potential flow field as well as the other required modules, described above.

1.5 Lewice

Lewice is an ice accretion prediction code that was developed by NASA engineers and several contractors, under NASA and FAA grants. The purpose of this program is to accurately predict ice accretion on different body shapes, in the widest range of meteorological and flight conditions. The ultimate goal of Lewice is to reduce the need for actual icing tests, and thus serve as a certification tool. In this section, the reader will be familiarized with Lewice abilities.

1.5.1 Lewice Structure

As explained in section 1.4.2, Lewice incorporates four independent modules. In the case of Lewice, the following models were used:

- The flow solver uses a 2D panel code (*S24Y*), developed by Douglas Hess-Smith, to calculate the potential flow field [11].

- The droplet trajectory module calculates the impingement points on the body, as well as the local collection efficiencies. This droplet trajectory calculation uses Langmuir's model [12].

- The mass and energy balance module, based on Tribus' model [13], predicts the local freezing fractions. The local densities are calculated following a model developed by Frost [28], based on the widely used Macklin correlation [14].

- The ice growth module computes the accreted body coordinates and assigns new panels to the body.

The computation process goes through each module, consecutively, each module providing the necessary information for the following one. Figure 1-6 shows the calculation process. Once the computer reaches the fourth module, a new body shape is generated. The computer is then ready to go through a new cycle of calculations for the following time-step.

1.5.2 Lewice Performance

Rime Ice Accretion

Lewice performs qualitatively well in the very cold ice accretion regimes at low LWC, were the ice is mainly rime and the ice shape is aerodynamic. In these cases, the local freezing fractions are unity and there is no runback. Figure 1-7 shows, side by side, the tracing of an ice accretion test on a NACA-0012 airfoil, and the result of an ice accretion simulation by Lewice: the overall ice shapes are similar.

Glaze Ice Accretion

In the glaze ice regime, Lewice does not perform as well (figure 1-8); the predicted ice growth is evenly distributed around the leading edge and around the impingement limits, while in the experiment, ice was found to accrete only around the impingement limits. To reproduce the experimental ice shape nonphysical values of surface roughness are often required. If no experimental data were available, Lewice, and most current ice accretion codes, could not correctly predict a glaze ice accretion. The adequate location of the boundary layer's transition to turbulence and accurate estimation of the convective heat transfer coefficient are crucial for the glaze ice accretion process. Numerous works have addressed these problems in the past years [15, 16].

Usually, in long enough exposures, glaze horns will develop aft of the transition region. As these horns grow, they increase their collection efficiency and heat transfer

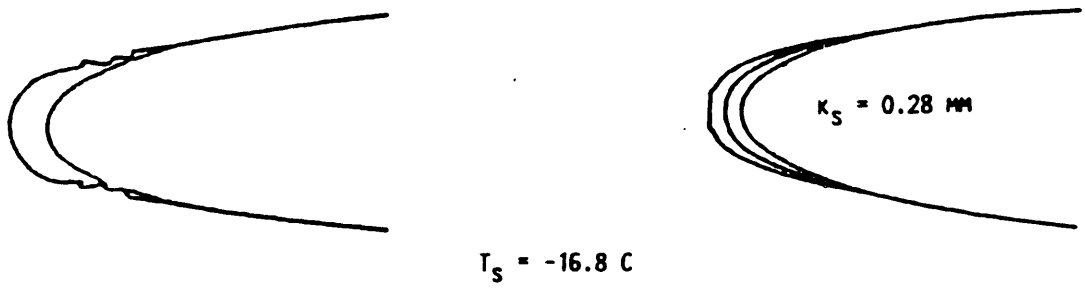

Figure 1-7: Lewice prediction (right) against IRT test result (left), for a rime accretion: Airspeed: 300 mph; MVD: 20 μm; LWC: 0.5 g/m^3 [21]

coefficients, accelerating their growth rate. Lewice has, in a few cases, qualitatively simulated this growth, by using unrealistic roughness and heat transfer coefficients, as previouslyy stated. The location of the transition to turbulence and the value of the heat transfer coefficients are dictated by the roughness height, in a way that will be described in chapters 3 and 4. In the turbulent boundary layer region, the heat transfer coefficient is greatly enhanced and the freezing fraction thereby augmented, causing a notable increase in the surface roughness and the ice growth rate.

Mixed Ice Accretion

The most difficult cases to predict are the ones that involve mixed ice accretion (figure 1-9). In these intermediate cases, zones of distinct growth types are observed. The variations of the convective heat transfer coefficient, along the iced surface, plays an important role. Accurate prediction of the transition to turbulence position is, therefore, required.

1.6 Motivation and Strategy

A better insight of the physical processes which occur during aircraft ice accretion is needed in order to improve Lewice predictions. Having had the opportunity to be

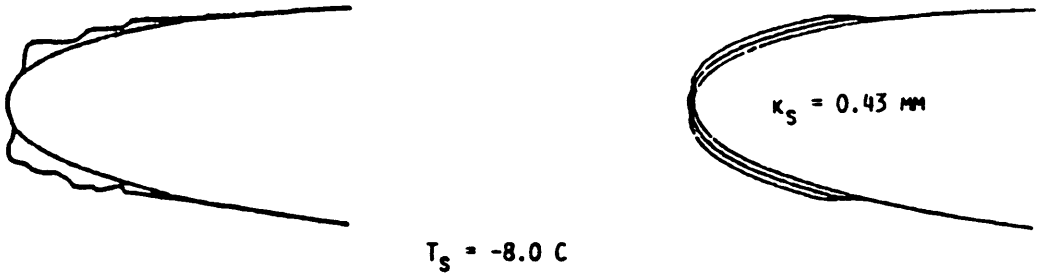

Figure 1-8: Lewice prediction (right) against IRT test result (left) for a glaze accretion: Airspeed: 300 mph; MVD: 20 μm; LWC: 0.5 g/m^3 [21]

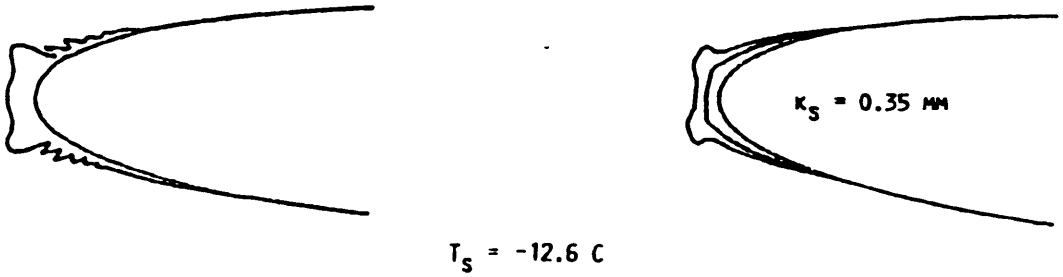

Figure 1-9: Lewice prediction (right) against IRT test result (left) for a mixed accretion: Airspeed: 300 mph; MVD: 20 μm; LWC: 0.5 g/m^3 [21]

involved in the conduction of icing tests at NASA Lewis' IRT, it was possible to put light on some microphysical mechanisms that govern the icing process. These icing tests swept the entire IRT performance envelop as described in chapter 2.

In addition, a set of preliminary wind tunnel tests was also performed at the Massachusetts Institute of Technology. The goal of these additional tests was to measure the effects of isolated roughness elements on the convective heat transfer coefficient. The technique used consisted in reading the surface temperatures of a roughened and heated flat plate, using infrared heaters and an infrared camera. Similar work have been performed in the past by French researchers at ONERA [7]. The present tests were performed with the collaboration of an icing specialist from ONERA, Dr. Robert Henry. The experimental set-up and the technique are described in chapter 3.

Several unresolved aircraft ice accretion aspects have been previously identified by Olsen [17] and included:

- Horn formation
- Different heat transfer regions
- Surface water behavior

In addition to these, more recent studies [18, 19] suggest the investigation of:

- Mixed ice accretions
- Rime feather growth
- Ice roughness formation mechanism

In chapter 2, the tests conducted at NASA Lewis IRT are presented with their results and analysis. Further testing at the MIT subsonic wind tunnel, are depicted in chapter 3, following the IRT tests. These *dry* experiments have given more insight on the discoveries of the IRT's close-up video tests. In chapter 4, results are applied to an enhanced physical ice growth model. Finally, in the concluding chapter, the author summerizes the tests observations and their implementation in the improved ice accretion model.

Chapter 2

Close-Up Video Icing Tests

In order to improve the ability of Lewice to accurately predict ice accretion processes, and in particular the formation of horns, closed wind tunnel icing tests were conducted. Those tests took place at the NASA Lewis Icing Research Tunnel, with the collaboration of NASA engineers and technicians. Close-up CCD cameras were used to monitor and record the experiments, and to allow for the observation of the ice accretion mechanisms occurring in each test. Both stagnation and off-stagnation regions were observed. The recorded images were then analyzed, and the results are presented at the end of this chapter. Two sets of tests were performed in the duration of the research. The first set of tests used two cylindrical bodies, while the second set of tests was performed on a laminar type airfoil.

2.1 Experimental Set-Up

The purpose of the wind tunnel icing tests was to capture the mechanisms of ice accretion, in general, and of horn formation in particular. To this effect, three to four CCD cameras were distributed around the test section. Simultaneous close-up and overview images of the ice accretion were recorded for later analysis. The observed regions were the stagnation line (close-up) and the horn regions (close-up and overview).

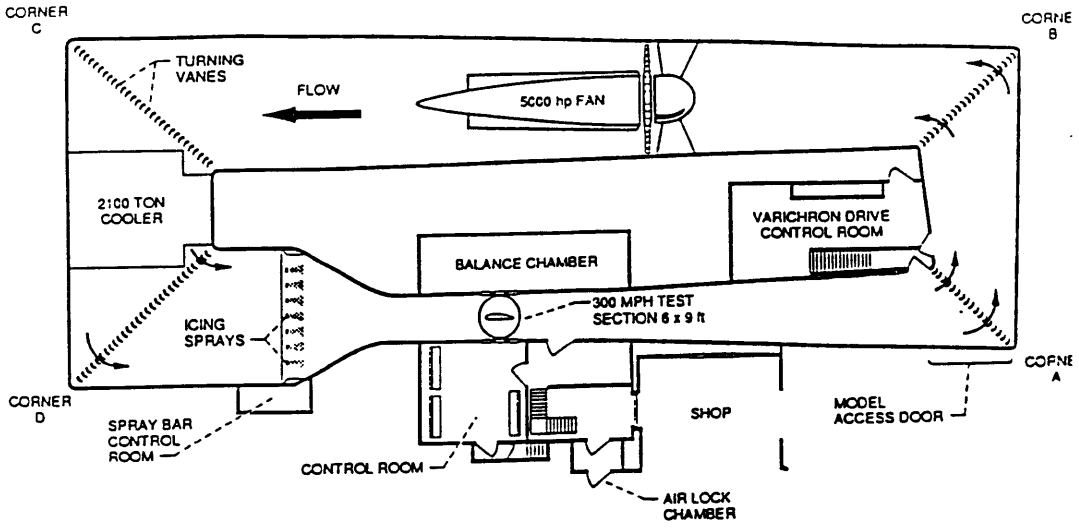

Figure 2-1: Detailed view of NASA Lewis IRT [22]

2.1.1 The Icing Research Tunnel

NASA Lewis' IRT is the world's largest refrigerated icing tunnel producing artificial icing clouds of varying severity. It is a closed-return atmospheric-type tunnel with rectangular cross section as shown schematically in figure 2-1. It is capable of varying its airspeed, in an empty test section, from 50 mph to 250 mph, and producing an air temperature from ambient temperature to -20°F. The dimensions of the tunnel test section are 6 ft high, 9 ft wide, and 20 ft long. It is equipped with spray bars and nozzles that produce supercooled water droplets of the size and concentration requested by the user. The tunnel performance maps of water droplet size as a function of liquid water content are presented in figure 2-2, for a range of test section velocities and two types of spray nozzles. The IRT control system was recently centralized into a computer network; it is now operated from an interactive color graphics, distributive control system.

2.1.2 Icing Test Models

For the sake of reducing the number of parameters in the analysis of the experiment, geometrically simple test models were chosen. For the first set of tests a 3.5 in diam-

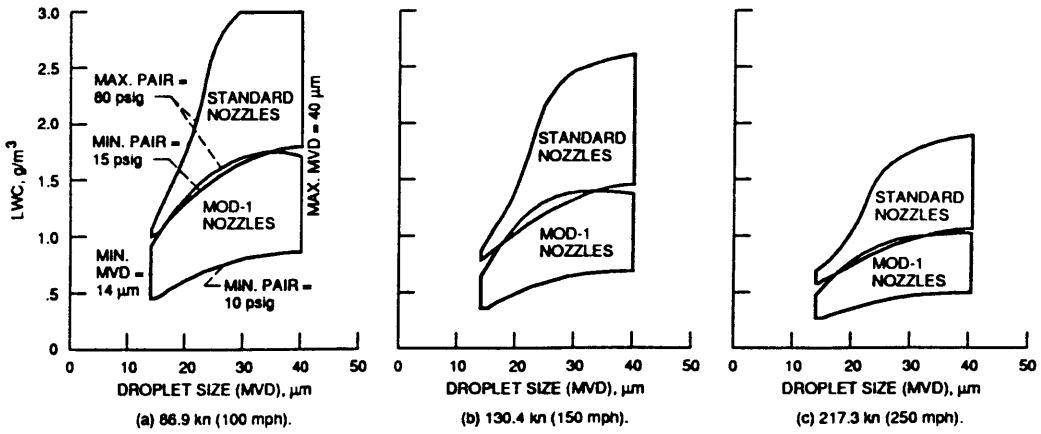

Figure 2-2: NASA Lewis IRT performance maps [22]

eter aluminum-skinned faired cylinder and a 2 in diameter aluminum cylinder were used. The aluminum-skinned cylinder was made of wood and had a thin aluminum sheet clamped on its surface.

In the second set of tests, an off-the-shelf fiberglass airfoil, designated MS(1)-317, was used. The test's objective was to further study the mechanisms of horn formation, in the case of an airfoil shape. The test matrix was focused on the expected glaze and mixed icing conditions, to study horn formation.

2.1.3 Video Camera Set-Up

CCD cameras were used for close-up observation of ice accretion in previous tests [18]. The camera and a strobe light, in these tests, were attached closely to the model to record close views of the freezing process. This set-up evolved from video imaging techniques originally used by Olsen and Walker [17].

For the cylinder tests discussed here, four CCD cameras were used, two of them with large magnification levels. The positions of the cameras are schematically presented in figure 2-3.

One of the cameras, labelled close-up floor camera in figure 2-3, was installed inside the test section, and protected by a faired assembly (figure 2-4). It was directed towards the stagnation region and mounted on motorized rails to allow for remote

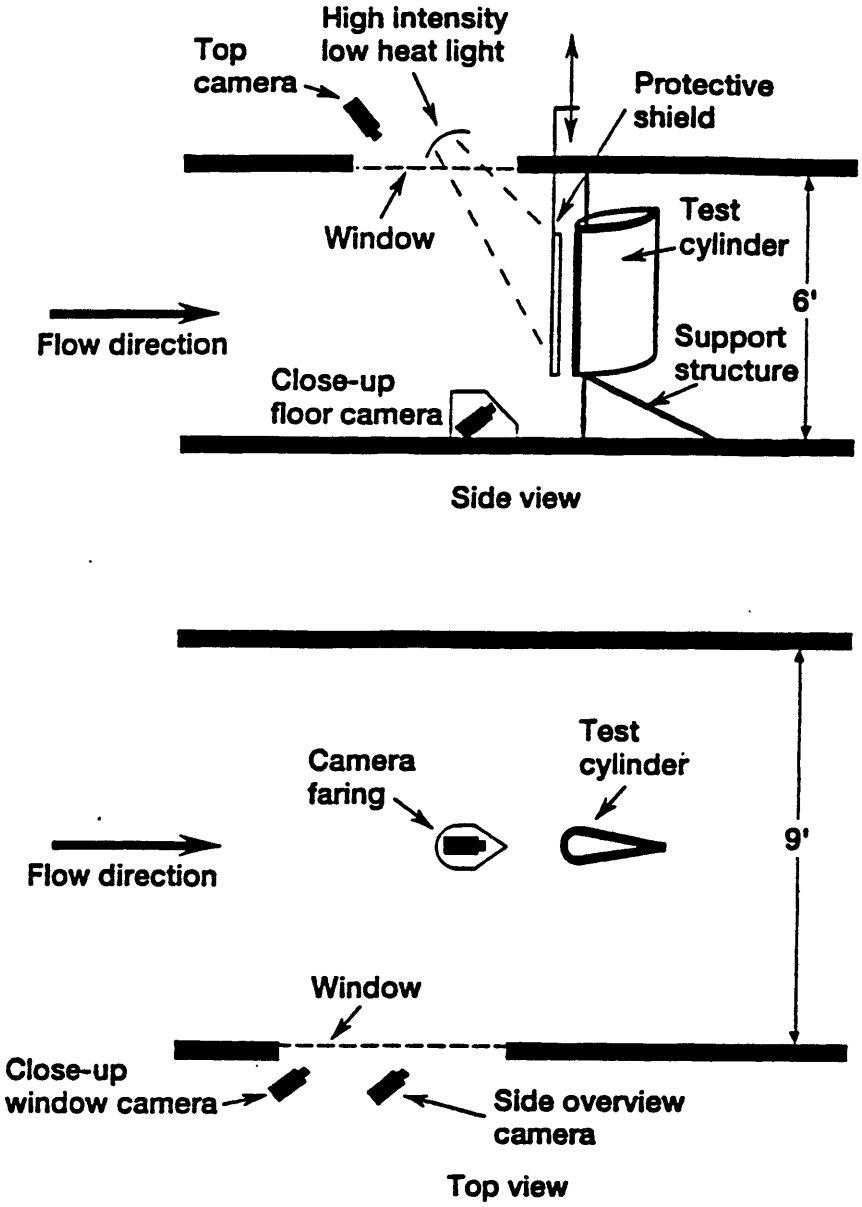

Figure 2-3: Close-up video icing tests set-up

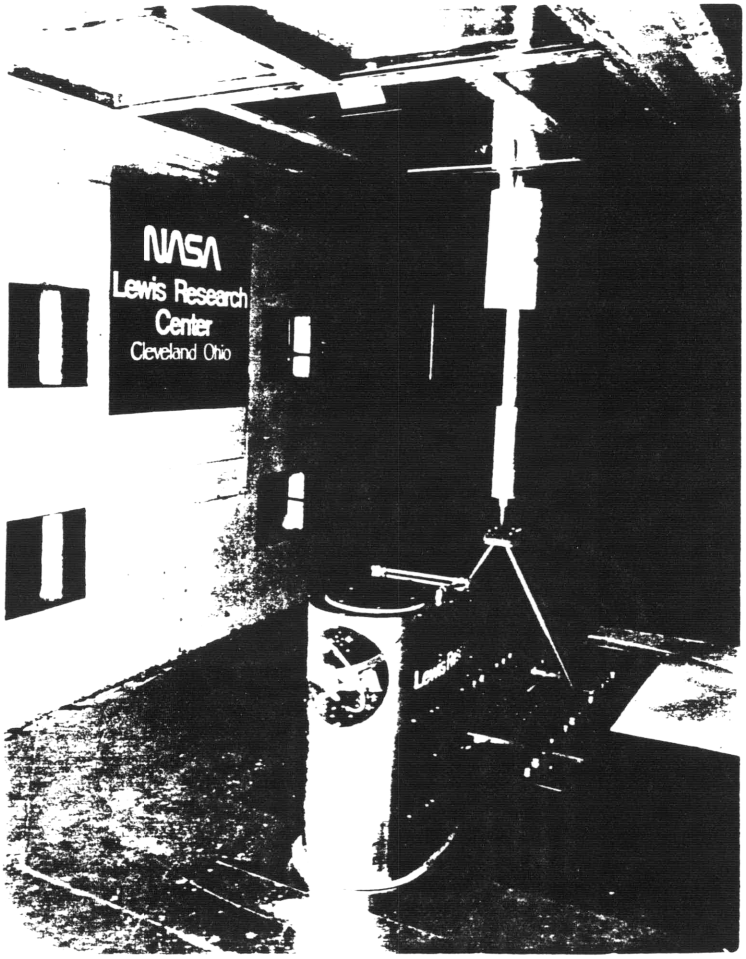

Figure 2-4: Picture of the test section

focusing (figure 2-5). This set-up could not tolerate vibrations from the cameras nor from the test model. The camera vibrations had to be damped, and the assembly isolated from the floor vibrations. In addition a flow of hot air was constantly fed inside the camera assembly to keep in the camera's operating temperature in a safe range. The window of the camera assembly was also heated with hot air, to ensure a clean camera field of view.

The other close-up camera was installed in the control room, monitoring the off-stagnation region through the side window of the tunnel test section. The purpose of this camera was to monitor the evolution of the surface roughness away from the stagnation region, and the formation of horns. Since the distance to the model was

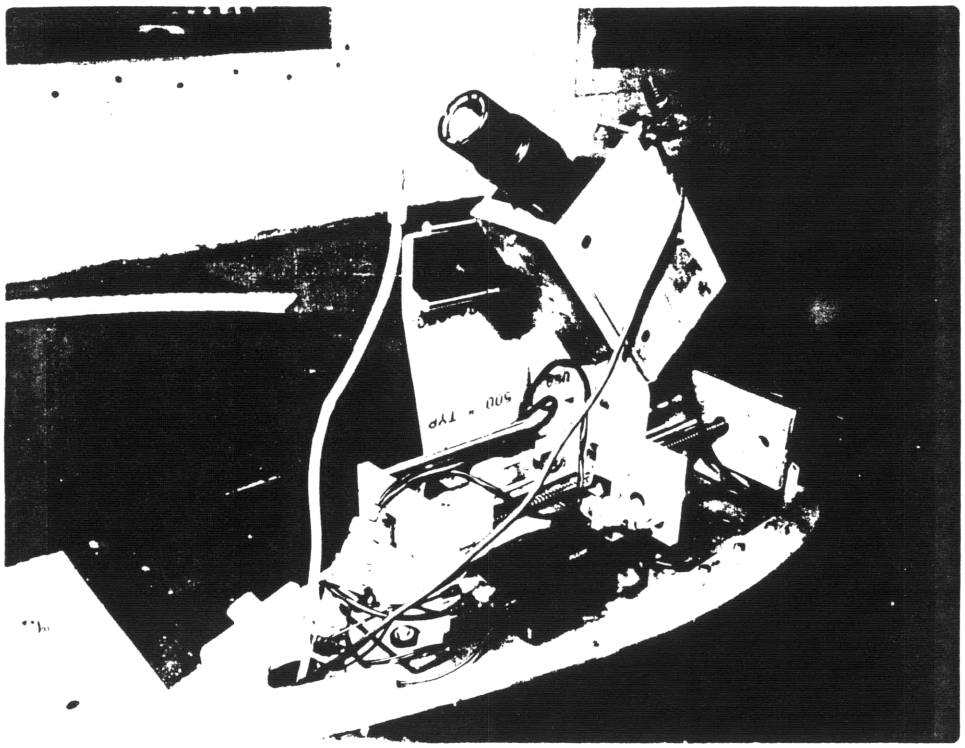

Figure 2-5: Picture of the stagnation camera focusing mechanism

greater for this camera a more powerful magnification lens was needed. By adding a sufficient number of extension tubes to a telephoto lens, a telescopic close-up lens was assembled (figure 2-6).

Two more CCD cameras were used for overall views of the model. One was mounted above the model, looking through the test section glass ceiling, while the other was mounted next to the telescopic close-up camera in the control room (figure 2-3). Simultaneous overall views were helpful in determining the nature of the processes occurring, while analyzing the close-up footage. In addition, the overview cameras allowed for the detection of anomalies during the tests.

Lighting was provided by a 575 W hydrargyrum medium-arc-length iodine (HMI) lamp, mounted above the test section ceiling. This external high power, low heat, illumination set-up limited the possibility of interference with the flow field and the ice accretion thermodynamics.

The video camera set-up in the airfoil tests was modified slightly to accommodate an even more powerful magnification lens for the stagnation close-up CCD camera.

Figure 2-6: Picture of the telescopic close-up lens assembly

The telescopic camera was installed above the glass ceiling of the IRT's test section, thus reducing the occurrence of vibration in the camera assembly, especially at high angles of attack. Consequently the HMI had to be installed beneath the test section floor, illuminating through a glass panel. This revised camera set-up allowed for more precise manual adjustment of the aperture and the magnification level.

2.1.4 Tests Procedure

The tests were conducted in collaboration with NASA Lewis IRT's technicians and engineers. The adopted procedure was the following:

A shield was lowered on the clean model to protect it from the undesired water droplets being shed off the wall, but also off the spray bars, before they reach an equilibrium operation. The wind-tunnel fan then accelerated to the desired speed while the air was cooled to the set temperature. When test airspeed and air temperature were reached the spray bars were activated and the nozzles started to spray droplets creating the required artificial icing cloud. The spray bars required a transient time to reach pressure equilibrium, during which the shield was kept lowered. When the

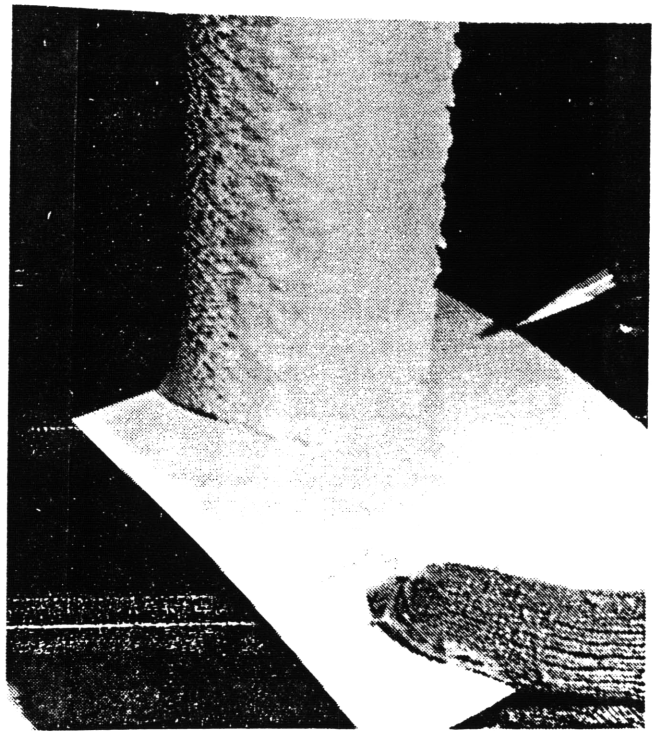

Figure 2-7: Cardboard and pencil ice shape tracing

pressure in the spray bars had all reached equilibrium that the shield was lifted and secured, and the SVHS recorders activated. During this time, the cameras were focused and adjusted if needed, and the test aborted if any severe anomaly, such as surface contamination or fogged camera, had occurred. At the end of the test, the video recorders were stopped and the wind tunnel airspeed set to idle, to allow for personnel's entrance in the test section. A cut was made in the ice accreted with a heated aluminum template. Then, a manual pencil tracing of the ice shape was carefully taken by aligning a cardboard template on the model (figure 2-7). In addition several still photographs were taken for further analysis. The model was then steam-cleaned and the shield lowered in position for the next icing test.

2.2 Icing Tests Matrices

The purpose of test matrix developed for the first set of icing tests, was to generate the widest possible range of test cases, within IRT's constraints, in the time allowed.

Parameter	Range
Velocity, mph	100, 150, 200
Temperature, °F	-15, -5, 5, 15, 25
Liquid Water Content, g/m^3	0.32, 0.5, 0.7, 0.75, 1.0
Mean Volume Diameter, μm	15, 20
Cylinder Diameter, in	3.5, 2

Table 2.1: Test matrix range for the cylinder tests

Parameter	Range
Velocity, mph	100, 150, 175, 200
Temperature, °F	5, 15, 25
Liquid Water Content, g/m^3	0.32, 0.5, 0.57, 0.67, 0.7, 0.75, 1.0
Mean Volume Diameter, μm	15, 20, 30

Table 2.2: Test matrix range for the airfoil tests

The 3.5 in aluminum skin faired cylinder was tested in a wide range of airspeed, temperatures, LWC and droplet sizes. The range of these parameters is listed in table 2.1. The second model in the cylinder tests, was tested less extensively, as its purpose was to examine the effect of the geometrical dimensions on the resulting ice shapes.

For the second set of tests, the purpose was to establish the processes that precede the formation of horns. Consequently the test matrix in this set was reduced to concentrate on the glaze and mixed ice accretion cases. The range of parameters tested in this experiment is listed in table 2.2.

2.3 IRT Test Observations

After analysis of the cylinder tests video recordings, that swept over the entire range of icing conditions available at the IRT, four types of ice accretions were observed (figures 2-8 - 2-11):

- Rime ice accretion: dry ice accretion, caused by the freezing on impact of the impinging water, due to low temperature and LWC. The resulting ice shape was aerodynamically shaped.

- Mixed ice accretion: glaze center and rime ice on the impingement limit region. Usually showed smooth surface in the glaze region, followed by a rougher mixed region and then rime feathers. The resulting ice shape was flat.

- Horns : two types of horn were identified;

  Horns labelled *Type A*: appeared in some mixed ice cases and seemed to grow inwards, in the local direction of the flow. They concurred with the presence of rime feathers in the outbounds of the accretion.

  Horns labelled *Type B*: identified in most pure glaze ice accretions. They tended to spread outward, and grow normal to the substrate.

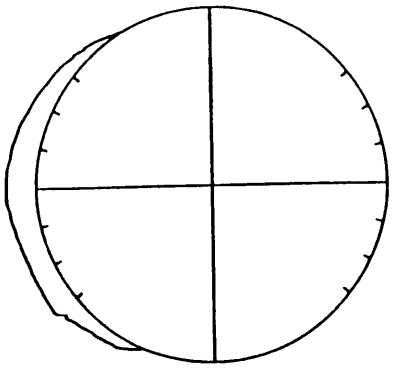

Rime

Figure 2-8: Rime accretion: Airspeed: 150 mph; MVD: 20 μm; LWC: 0.5 g/m^3; Temperature: -15 °F

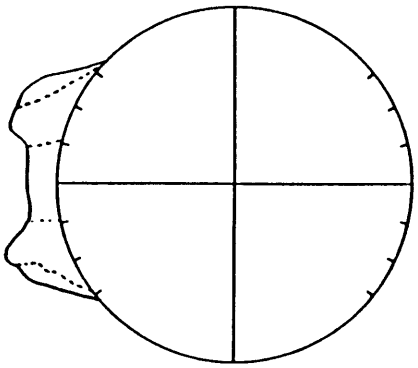

Horn A

Figure 2-10: Type A Horn: Airspeed: 200 mph; MVD: 15 μm; LWC: 0.5 g/m^3; Temperature: 25 °F

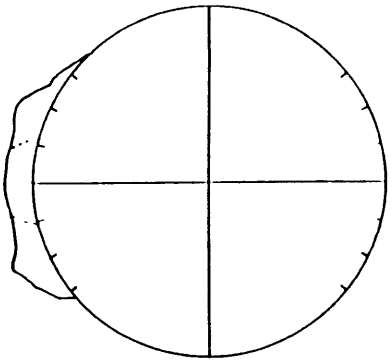

Mixed

Figure 2-9: Mixed accretion: Airspeed: 200 mph; MVD 15 μm; LWC: 0.32 g/m^3; Temperature: 25 °F

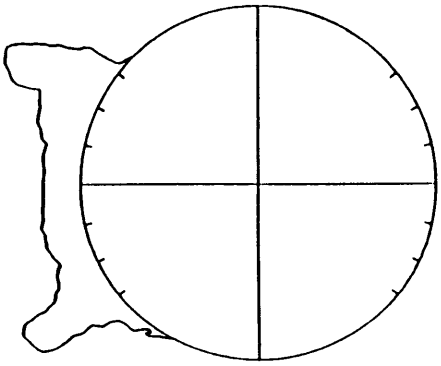

Horn B

Figure 2-11: Type B Horn: Airspeed: 150 mph; MVD: 20 μm; LWC: 1.0 g/m^3; Temperature: 25 °F

Feather Growth Observations

It was noted, especially during the analysis of the video images, that in rime and mixed ice accretion regimes, small discrete rime growths occurred. In all rime ice accretions, these small rime growths occupied all of the accreted region. In mixed ice accretions, the same small dry growths were observed in all the accreting regions, except close to the stagnation line, where wet growth had formed. These distinct ice accretions had a small cross section and were densely distributed, particularly at low LWC, low temperature and high airspeed. They grew in the direction of the flow, in an inverted conical shape, with an opening angle of around 30^o to 50^o. This kind of rime growth was known to occur at the impingement limits, in a larger scale, and were referred to as *feathers*. Figures 2-12 - 2-16 show pictures of discrete small feathers from the tests being discussed here, at different stages of growth. Also visible in figures 2-12 - 2-16 are the *interstitial gaps* between distinct feathers; because the feather cross sections increased as more ice accreted, large gaps developed at the root of the feathers. These interstitial gaps resulted in the low mass density of rime accretions. In very cold rime regimes, feathers were especially dry and brittle, and shedding of whole or part of feathers was observed.

The feather growth mechanism was thoroughly investigated and played a key role in the formulation of the new ice accretion model. The analysis of the feathers observation is presented in section 2.4.

Observations of Surface Water Behavior

Another phenomenon noted in the IRT tests, and already mentioned in recent work [17], is the fact that the unfrozen water in most of the ice accretion tests, did not runback, but stagnated in pools. At the very beginning of a typical mixed or glaze ice case, when the flow was thought to be laminar, the water ran in rivulets. If the flux of water were high and the temperature close to the freezing point, a film of water could even have formed over the stagnation region and somewhat beyond. Then some of the water froze as the roughness increased. The unfrozen water was trapped in small stationary pools. This final stage could be identified as the steady-state behavior of

surface water. This is an important finding, since most of the ice accretion models, assumes that the unfrozen water runs back along the body until it freezes or it is shed.

This behavior of the water helps explain, the different roughness zones on typical glaze and mixed ice accretions. The stagnation region, experiencing a very low freezing fraction, has a lot of water running back, and actually may be constantly covered by a film of water. Close-up analysis of ice samples at the end of runs, revealed that the region neighboring the stagnation line of the accretion was very smooth. The water film easily accounts for that. In glaze ice accretions, the stagnation region was generally followed by a rougher region, where little ice roughness elements appeared.

Transition to Turbulence Observation

It was not always possible nor easy to observe transition to turbulence on ice accreting surfaces. To observe transition, the tests' video tapes had to be visualized many times at lower speeds. In the case of pure glaze ice, transition, or at least what appeared to be the advancement of a *front* of higher heat transfer coefficient, was clearly visible. At the beginning of pure glaze test cases, water runback was abundant. Slowly, and starting from behind the impingement limit, the rivulets of water froze partially. The inbound limit of the frozen water then migrated slowly towards the stagnation region. The frozen front eventually settled at about 2 cm of the stagnation location, in most glaze cases involving the 3.5 in cylinder.

2.4 Analysis of Feather Formation

Feather Growth Mechanism

Rime feathers were observed in all rime ice accretions. Actually, in all observed cases, rime ice appeared to be formed of ice accreted through discrete feather formation. This conclusion was reached by looking at the rime accretion close-up video images and at still photographs as in figures 2-12 - 2-16. These feathers accreted only inside the impingement limits, supporting the assumption that rime feathers are formed by

droplets freezing on impact. Moreover, in cold rime ice accretions, no ice accreted beyond the impingement limits.

When accreted under cold temperatures or at low LWC, the rime ice structure was brittle, and shedding occurred. This helps explain the smooth and aerodynamic final overall shape of rime accretions (figure 2-8).

In mixed ice accretion cases, feathers were still observed, except in the very central part of the stagnation region. The feathers density (number of feathers per unit area) was lower than in the rime cases.

It was noted, if initial surface roughness was present, that feathers grew out of the ice roughness elements. If the surface was initially smooth, feathers appeared at a later stage of the ice accretion process, but at a higher density. When initial roughness was present, feathers started growing right away. In all cases, by analyzing the video tape recordings, feathers can be traced back to the initial contamination site. The nucleation sites were roughness elements which experienced higher local convective heat transfer coefficients. These protuberances started to outgrow the boundary layer, as their growth rate increased, enjoying the local free stream velocity and a larger water catch. The freezing fraction on the tip of such surface roughness was such that impinging water frozen on impact while, at their root, inside the boundary layer, water was observed.

Tracing of typical feathers were performed using the video tapes. Figure 2-17 shows a tracing of an observed growing feather at 20 seconds time intervals. Feather growth on electrical wires was studied by Personne [23], who subsequently developed a ballistic model for rime growth. In Personne's ballistic model, water droplets are accumulated on each other as they impact on the body. Figure 2-18 is extracted from Personne's work. The similitude of the observed feathers with the ones that Personne [23, 24] identified in its low speed tests, and predicted in his ballistic model, is remarkable.

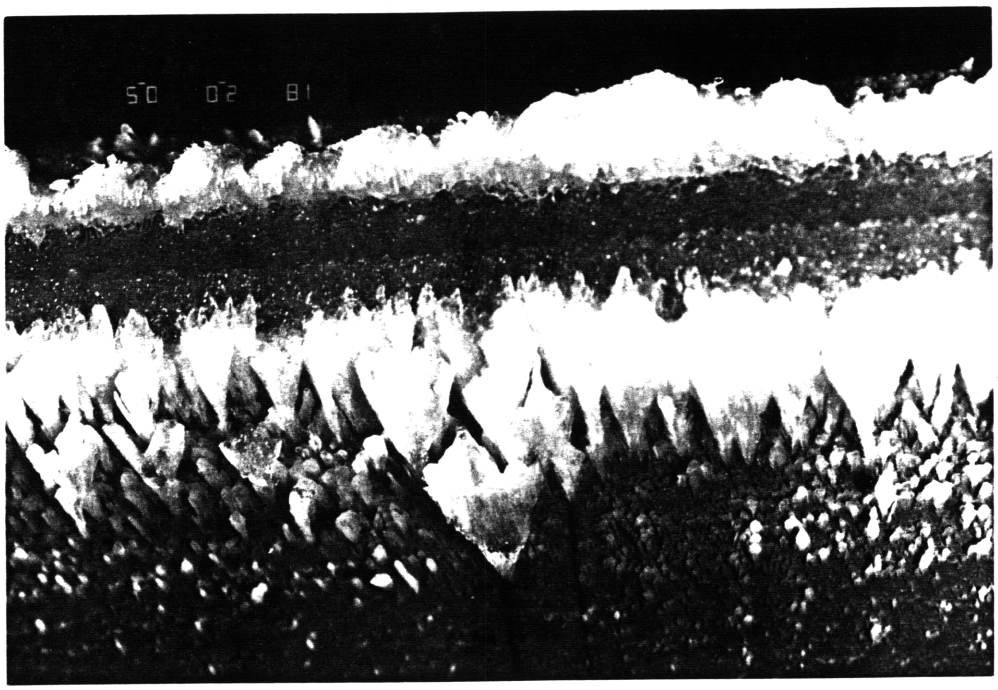

Figure 2-12: Rime feathers: Airspeed: 200 mph; MVD: 15 μm; LWC: 0.5 g/m^3; Temperature: 25 °F

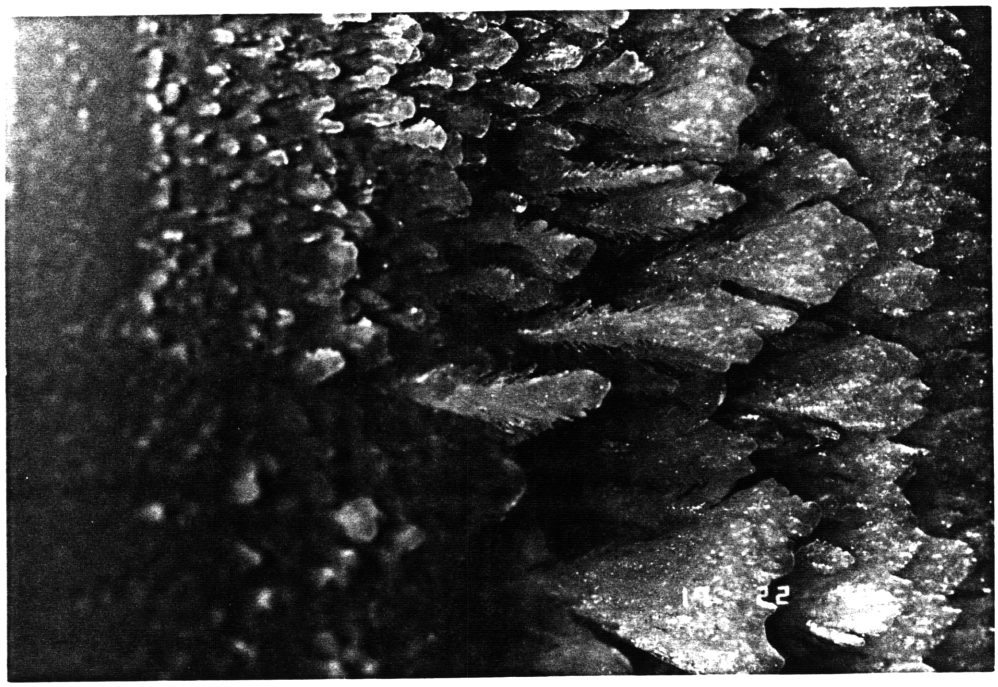

Figure 2-13: Rime feathers: Airspeed: 200 mph; MVD: 15 μm; LWC: 0.32 g/m^3; Temperature: 25 °F

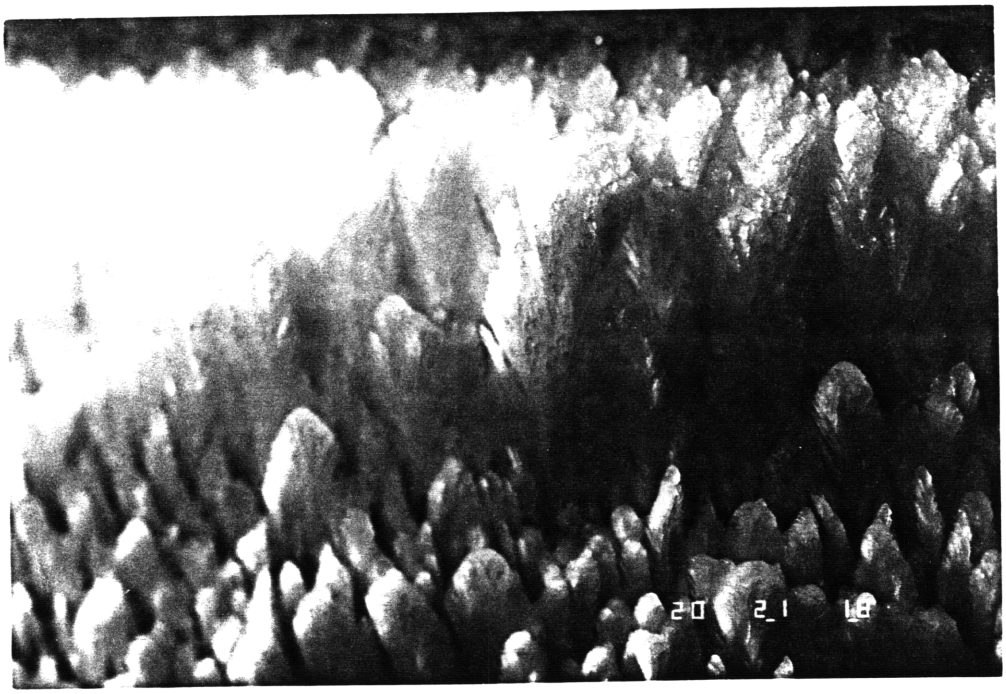

Figure 2-14: Rime feathers: Airspeed: 150 mph; MVD: 20 μm; LWC: 0.75 g/m^3; Temperature: 5 °F

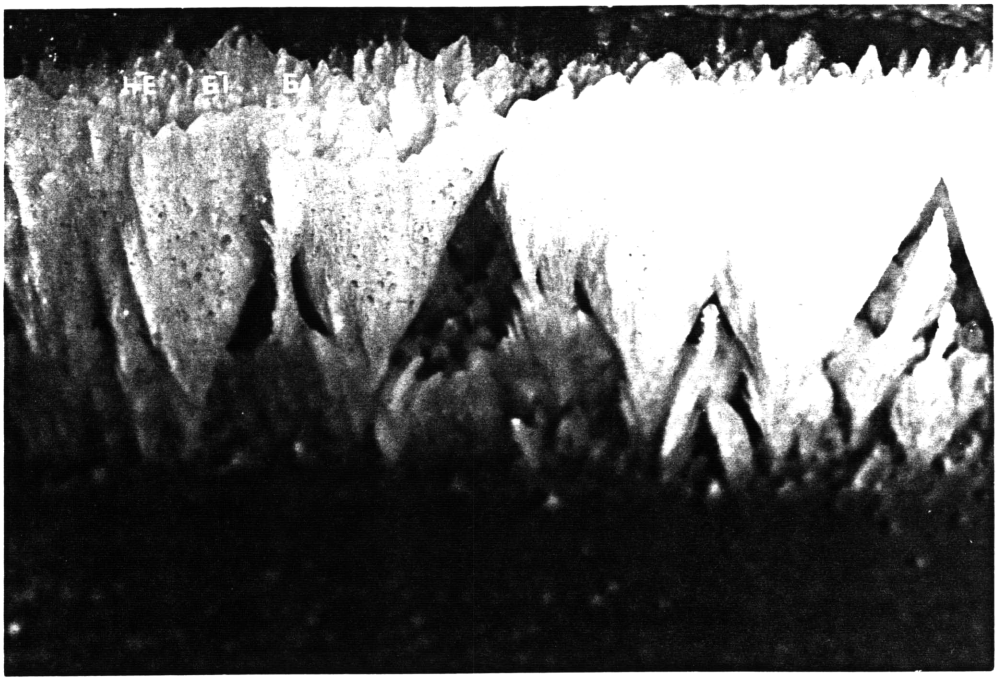

Figure 2-15: Rime feathers: Airspeed: 150 mph; MVD: 20 μm; LWC: 1.0 g/m^3; Temperature: 15 °F

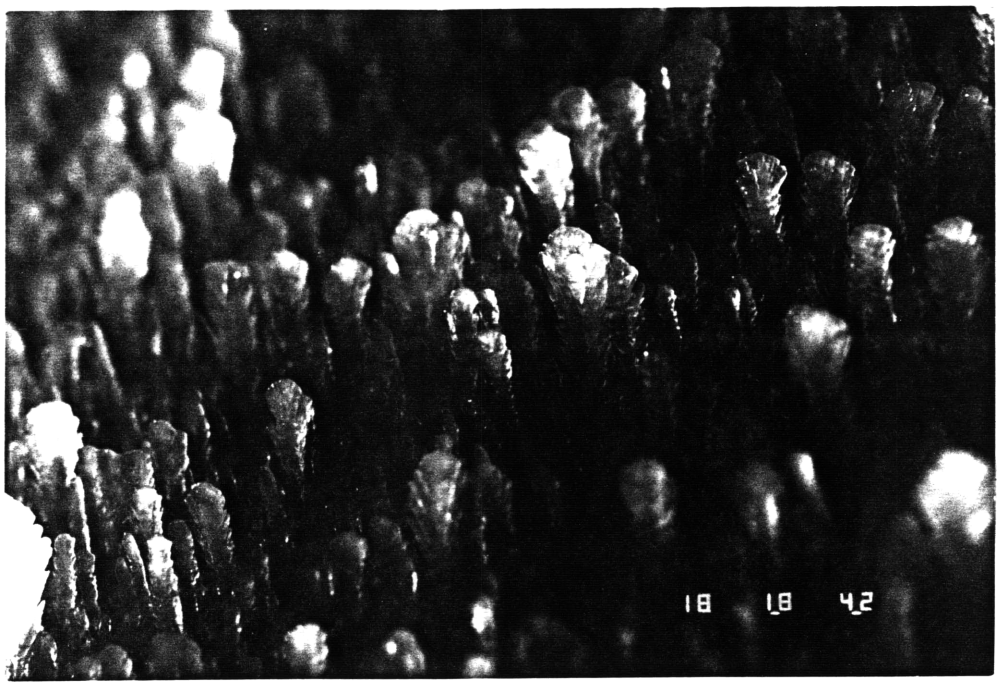

Figure 2-16: Rime feathers: Airspeed: 150 mph; MVD: 20 μm; LWC: 0.75 g/m^3; Temperature: 25 °F

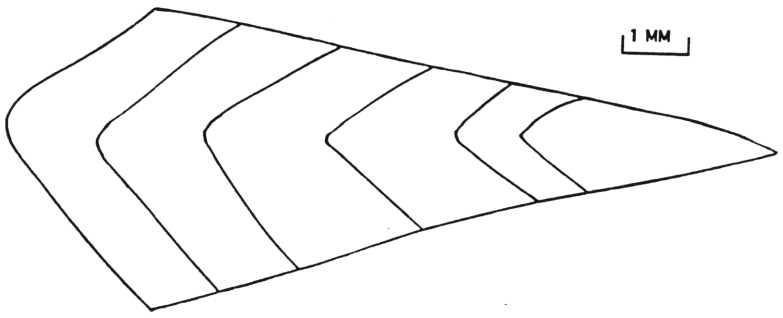

Figure 2-17: Observed feather shape at 20 sec intervals: Airspeed: 100 mph; MVD: 15 μm; LWC: 0.7 g/m^3; Temperature: 25 °F

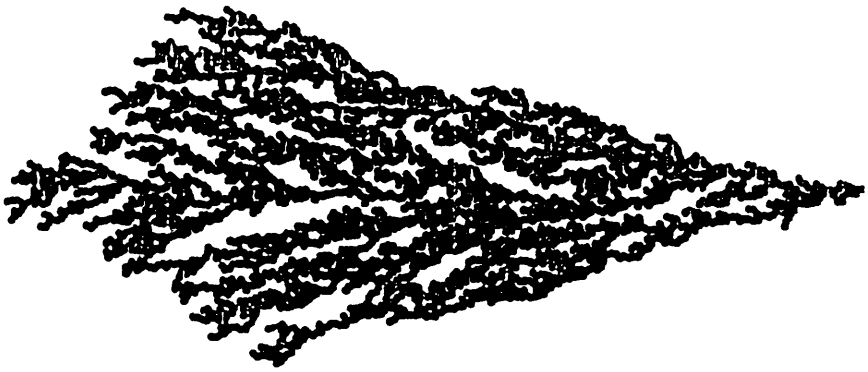

Figure 2-18: Feather shape as predicted by Personne's ballistic model [24]

Feather Rate of Growth

The rate of growth of the feathers in different ice accretions were measured from the video tapes. The rate of growth of the feathers appeared to depend mainly upon the total mass flux of impinging water that the body collected (figure 2-19). This flow of water can be approximated by equation 2.1:

$$\dot{M} = LWC \;\; V \tag{2.1}$$

Feather growth for different water mass flux are presented in figures 2-20 - 2-24. After a slow start, the growth appears to be linear in time. The feathers that grew well above the boundary layer thickness exhibited a very high growth rate. In some cases, feather growth was effected by the presence of an upstream feather that blocked the water flux. These blockages explain the slow initial feather growth, until the feather reaches out. The steady-state growth rate of the feathers is presented in figure 2-25. The growth seems to be linear with respect to the water mass flux, but the accuracy and number of data available did not allow for a definitive statement.

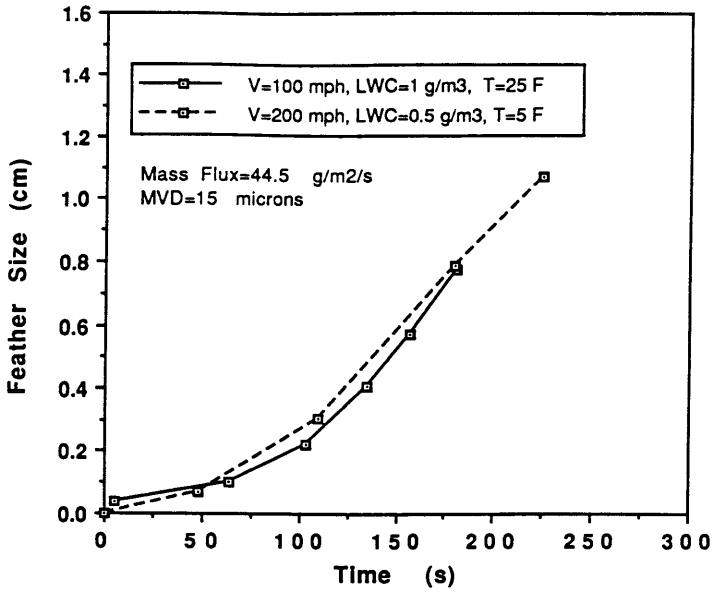

Figure 2-19: Measured feather growth for two test cases with constant water mass flux

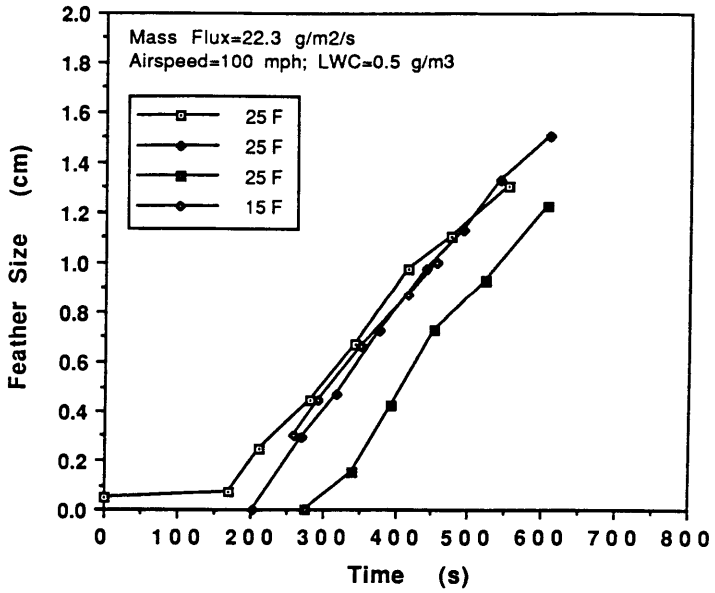

Figure 2-20: Rime feather growth: mass flux of 22.3 g/m^{2}s

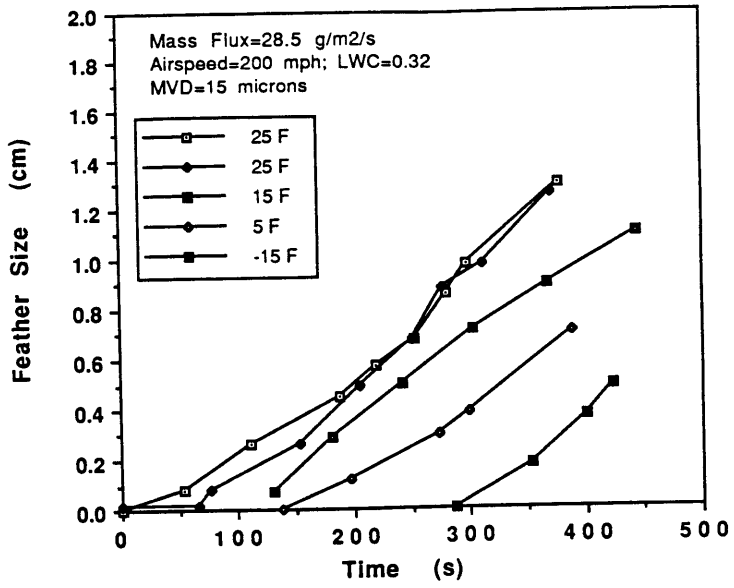

Figure 2-21: Rime feather growth: mass flux of 28.5 g/m^{2}s

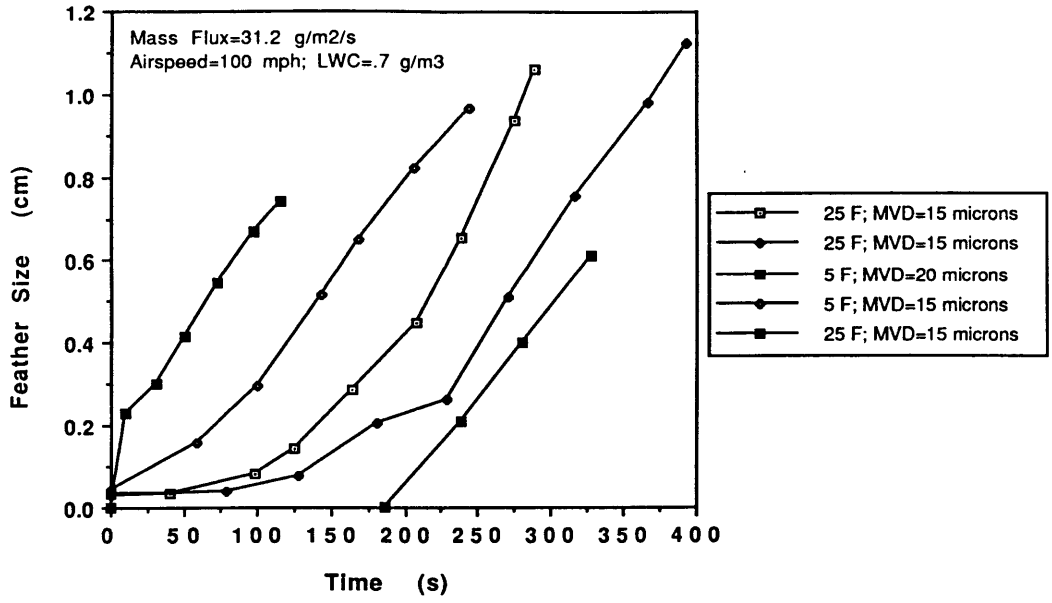

Figure 2-22: Rime feather growth: mass flux of 31.2 g/m^{2}s

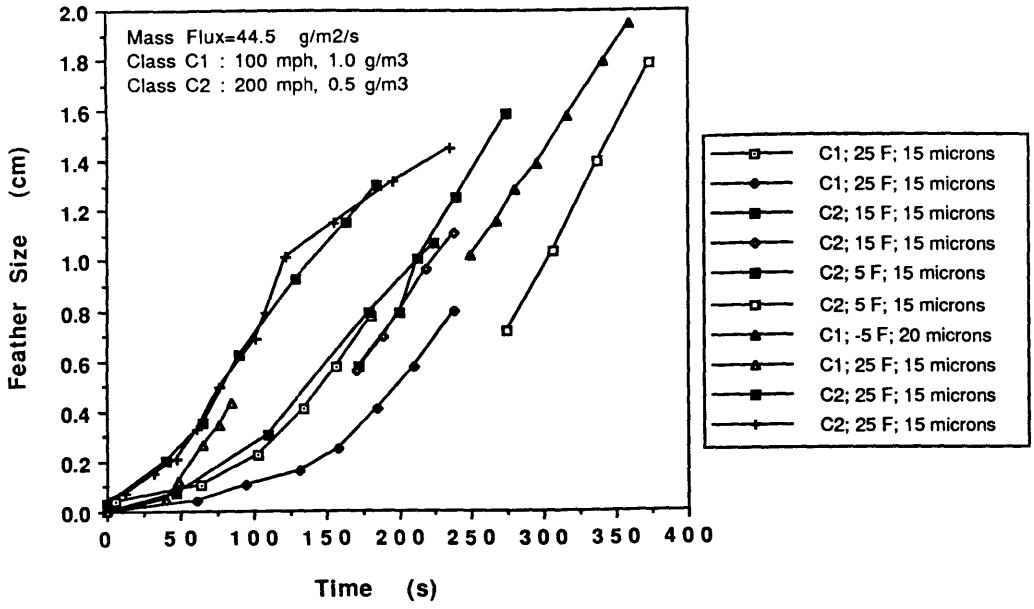

Figure 2-23: Rime feather growth: mass flux of 44.5 g/m^{2}s

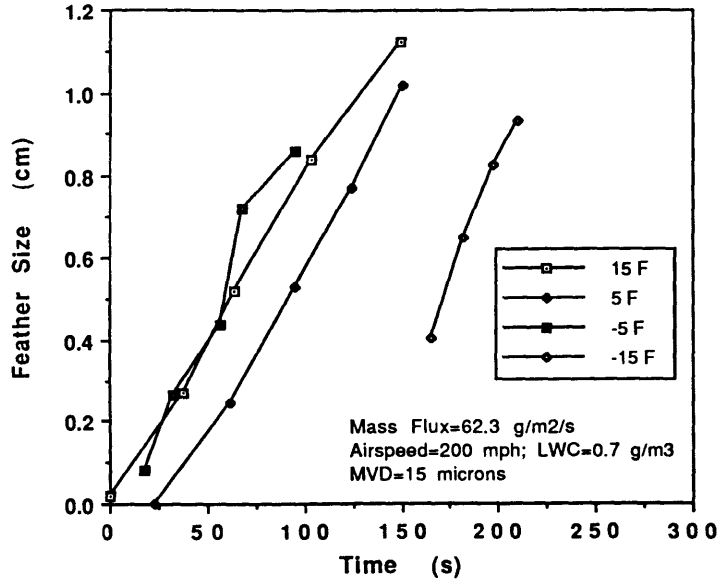

Figure 2-24: Rime feather growth: mass flux of 62.3 g/m^{2}s

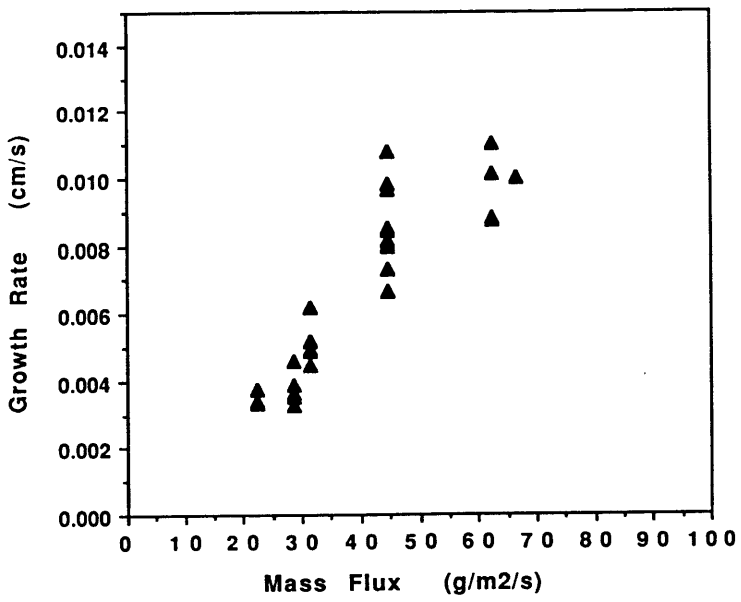

Figure 2-25: Observed steady state feather growth for a variety of operating conditions

2.5 Analysis of Horn Formation

As stated earlier two different kinds of horns were observed in the range of conditions tested; *Type A horns* and *Type B horns.* The following is a detailed account of the horns formation mechanisms observed through the close-up video images.

Type A Horns

Type A Horns were observed in selected mixed ice accretions. These horns were made of mixed ice, and grew in the direction of the flow. They were formed at the end of the glaze ice accretion region, where the high surface roughness was favorable for feather growth.

In a typical case of mixed ice accretion, the video data showed that excess water on the surface ran back, starting from the stagnation line. After a few seconds of exposure, the amount of running water diminished and roughness developed on the surface. At the limits of the impingement region, rime feathers were observed to grow. The upstream edge of the feather region moved slowly towards the stagnation region. Some water still ran back in the form of rivulets, in-between the roughness, filling the

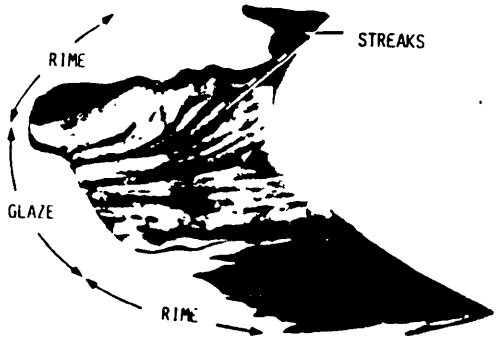

Figure 2-26: Backlit view of a mixed ice accretion [17]

interstitial gaps between the feathers. This reinforced the feather roots and limited the amount of ice shedding. In some mixed ice cases the feathers continued to grow and formed Type A horns. In other mixed cases, the growth stopped prematurely, leaving a mixed ice accretion with no horns, and a rather flat frontal area.

One possible explanation for the stop in growth, is to note that typically the tip of the feathers became more wet, and then carefully conclude that the interstitial gaps had all been filled with runback water. The incoming runback water was observed to flow on the top of the feathers, reducing the freezing fraction and paralyzing the feather growth.

A backlit image of a mixed ice accretions cut, from the work of Olsen and Walker [17], supports this theory. The streaks in the inside of the mixed region show the direction of the feather growth, while the absence of air bubbles is explained by the interstitial filling process (figure 2-26).

Type B Horns

Type B horns were observed in most glaze ice accretions. They were formed in the rough glaze ice surface, away from the stagnation line. These horns were fed by runback water and grew normal to iced surface.

Type B horns were produced by the freezing of runback water, where the local freezing fraction was high, but still under unity. The freezing process is governed

mainly by the local heat transfer coefficients, that in return are dictated by the surface roughness. At the beginning, water flows abundantly in the form of a film until, very shortly, roughness forms downstream. This is thought to occur right after the boundary layer is tripped to turbulence. The enhanced convective heat transfer coefficient, due to the turbulent flow, allows for more water to freeze and thus more roughness to be generated. Yet the freezing fraction does not approach unity and therefore no feathers form. Instead, a glaze horn slowly forms.

As the droplet sizes increased, the location of the glaze horns, migrated downstream. Figure 2-27 shows different tracings of horns for the same overall conditions but different MVD's. As the droplets size was increased, the trajectory of the droplets straightened, and thus less water evaded the body. As a result, the horns grew further aft on the body, where the heat transfer coefficient was higher and the freezing fraction closer to unity. Note that for the 15 μm case a Type A horn was observed, while in the higher MVD cases, Type B horns formed.

Unlike Type A horns in the mixed cases, Type B horns were observed on all pure glaze accretions, giving the required amount of time, in the range of conditions tested. The horns, and the other regions of the glaze ice accretions, had accreted in a direction *normal to the surface.*

2.6 Analysis of Transient Water Behavior

This phenomenon had already been observed in previous experiments, and different roughness zones were identified [20, 26]. The most probable explanation for the migration of this freezing front is that the generated roughness induced a higher heat transfer coefficient, which, in return, allowed more water to be frozen. The frozen roughness progressed until the point, close to the stagnation region, where the flow was so slow that the heat transfer could not freeze the water. This limit is thought to be the transition to turbulent line, and the front progression in the first instants of the accretion, its transient position. Figure 2-28 shows a schematic representation of how the surface roughness advanced, and the transition border proceeded towards

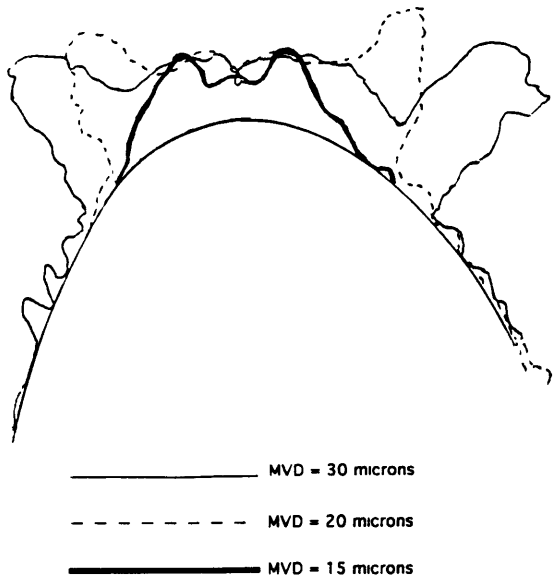

Figure 2-27: Variation of horn position with MVD: Airspeed: 200 mph; LWC: 0.7 g/m^3; Temperature: 25°F

the stagnation region.

2.7 Implications for Ice Accretion Modeling

The single most important result of the icing tests, is the discovery of the prevalence of feathers formation in all nonpure glaze ice accretions. These feathers grow in the local direction of impingement, within the impingement limits. The Lewice routine for ice growth allows only for growth normal to the surface. Lewice is therefore unable to predict feather growth. Furthermore, feathers not only formed in the impingement limits of the accretion, as previously thought, but also inside most of the impingement limits. This observation has serious implications with respect to the present ice growth model.

The following is a list of the phenomena encountered that are thought to have a direct effect on the modeling of ice growth:

- When the local freezing fraction reaches unity, the impinging water can freeze as feathers, and grow ice in the local direction of impingement. Type A horns

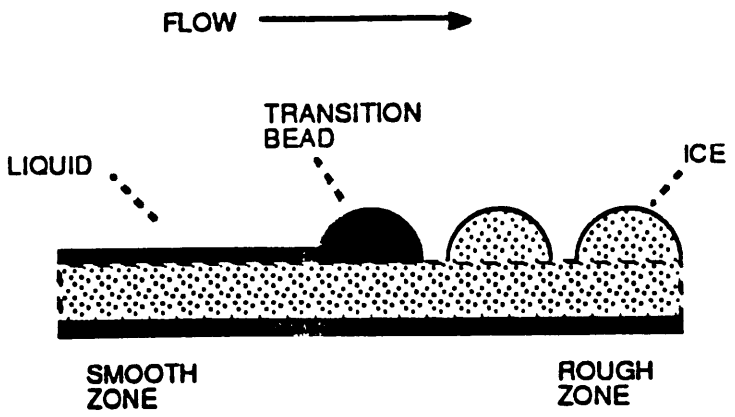

Figure 2-28: Freezing front progression mechanism [16]

might subsequently form. The new model should allow for ice growth *in the impingement direction*, in the feather region.

- The water running back, in presence of feathers, fills in gaps between feathers and freezes instead of simply freezing on top of the ice surface. The density of the ice accretion can therefore be altered. The new model should also allow for this mechanism.

- The feathers experience a different flow as they rise above the surface of the ice, and sometimes well beyond the local boundary layer height. The model should also include a special set of values for the convective heat transfer coefficient on the tip of the feathers.

- As unfrozen water actually stagnates most of the accretion time, excess water should be allowed to stay on a panel and not always move to the next one.

- Several roughness zones were observed in glaze and mixed ice accretions. Lewice should be run with different roughness zones in these cases.

Chapter 3

Dry Roughness Tests

Discrete feathers were identified in rime and mixed ice accretion regimes, as discussed in chapter 2. Individual feathers were observed to grow out of small ice roughness elements. Very soon, they outgrow the boundary layer, thanks to an increased local convective heat transfer coefficient. In order to accurately model this growth, more information is required on the behavior of the local heat transfer coefficients on a roughness size comparable to the boundary layer height.

In this chapter, a *dry* wind tunnel experiment, to quantify the enhancement in local heat transfer coefficient due to individual roughness or feather, is presented. These tests were conducted by Dr. Robert Henry with the assistance of the author [7, 29].

3.1 Experimental Technique

The technique used in this experiment relied on infrared thermography, visualization of surface temperature through an infrared camera (figure 3-1). The surface temperature of roughness elements on a flat plate, was increased by heat radiation from an infrared lamp. The infrared camera then captured the heat emissions $\dot{Q}_r$ from the heated body and, via an integrated calibration system, displayed the temperature map of the body surface. The body was made of nonconducting material so that heat loss by conduction was negligible. In addition, the body surface had a nonreflective

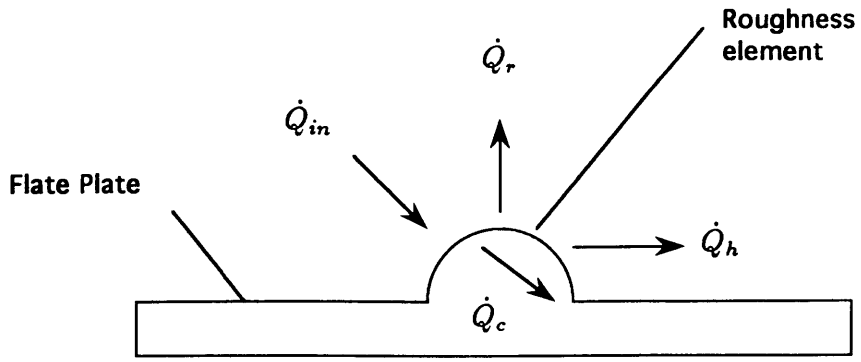

Figure 3-1: Schematique presentation of the experimental technique

coating.

In steady-state, the radiative flux hitting the body $\dot{Q}_{in}$ is equal to the sum of the heat radiated out of the body $\dot{Q}_r$, the heat conducted through the body $\dot{Q}_c$ and the heat added or removed by convection $\dot{Q}_h$, as expressed in equation 3.1. In the case of the tests discussed here, the heat loss by conduction $\dot{Q}_c$ was minimized by the use of nonconducting materials. In addition, in the range of operating temperatures, the heat that the body radiated $\dot{Q}_r$ was much smaller than the heat added to it, $\dot{Q}_{in}$. Therefore, the heat added to the body was approximately equal to the heat extracted by convection, as expressed in equation 3.2.

Since only the local *increase* in convective heat transfer coefficient was of interest, the amount of heat introduced in the system was not required in the technique. This increase was calculated by comparing the temperature reading in the perturbed area (equation 3.3) containing the roughness element, to the temperature in an unperturbed reference point (equation 3.4), as expressed in equation 3.5 and presented in figure 3-2.

$$\dot{Q}_{in} = \dot{Q}_r + \dot{Q}_c + \dot{Q}_h \tag{3.1}$$

$$\dot{Q}_{in} = \dot{Q}_h = h(T_{surf} - T_a) = h(\Delta T) \tag{3.2}$$

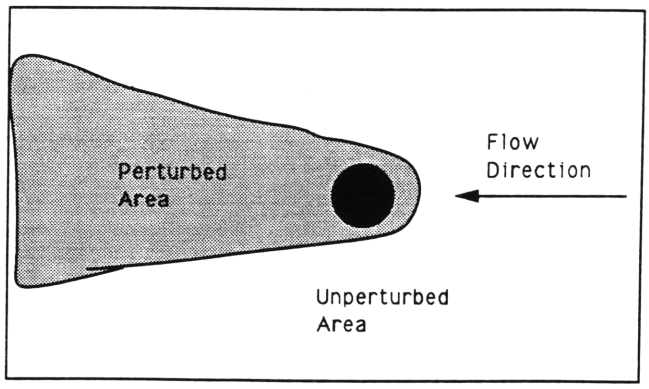

Figure 3-2: Perturbed and unperturbed zones

$$\dot{Q}_{in} = h_{perturbed}(\Delta T)_{perturbed} \tag{3.3}$$

$$\dot{Q}_{in} = h_{unperturbed}(\Delta T)_{unperturbed} \tag{3.4}$$

$$\frac{h_{perturbed}}{h_{unperturbed}} = \frac{(\Delta T)_{unperturbed}}{(\Delta T)_{unperturbed}} \tag{3.5}$$

3.2 Experimental Set-Up

A flat plate with *beadlike* roughness elements was tested in a low speed 1ft x 1ft wind tunnel, to measure the changes of the heat transfer coefficient under laminar and turbulent boundary layer conditions. To this effect, a simple method using heaters and an infrared camera was developed. The following is a description of the experimental apparatus.

The Test Model

The test model consisted of a 1/2 in thick flat plexiglass plate. Test roughness elements were glued on the plate in the infrared camera field of view. The leading edge

of the plate was carefully rounded, to assure a laminar flow at the low test airspeeds. For the turbulent boundary layer tests, a thin wire was placed at the leading edge to trip the boundary layer. The flat plate and the roughness elements were painted in flat black, to avoid parasitic heat reflection and ensure homogeneous heating. The roughness elements and the plate itself were made of plastic materials to reduce heat loss by conduction. The dimensions of the plate are presented in figure 3-5.

The Heating System

The heating elements used for the tests were three infrared lamps of 250 W each. The three lamp heating system, evenly distributed just over the plexiglass upper wall of the wind tunnel (figures 3-3 and 3-4), was found to be effective for the geometry and space availability of the experimental set-up. Cooling for the upper wall of the plexiglass test section was necessary to avoid melting, and was provided by a small fan.

The Temperature Sensing System

An infrared camera (Hughes) was used to map the surface temperatures of the test element. The minimal resolution required to distinguish different heat transfer zones on a typical roughness, was of the order of a fraction of a millimeter. The infrared camera was found to have a resolution higher than half a millimeter, when used at a distance of 15 cm, which was half the test section height. Consequently, the camera was located above the plate, on top of the squared test section, facing down towards the roughness elements, as shown in figures 3-3 and 3-4. The camera's field of view in this configuration was of 3 cm x 5 cm.

Additionally, three thermocouples were incorporated in the plate, in the field of view of the infrared camera, to verify the accuracy of the surface temperature readings. Another thermocouple was maintained in the freestream, at the test location, to measure the freestream temperature needed in equation 3.5.

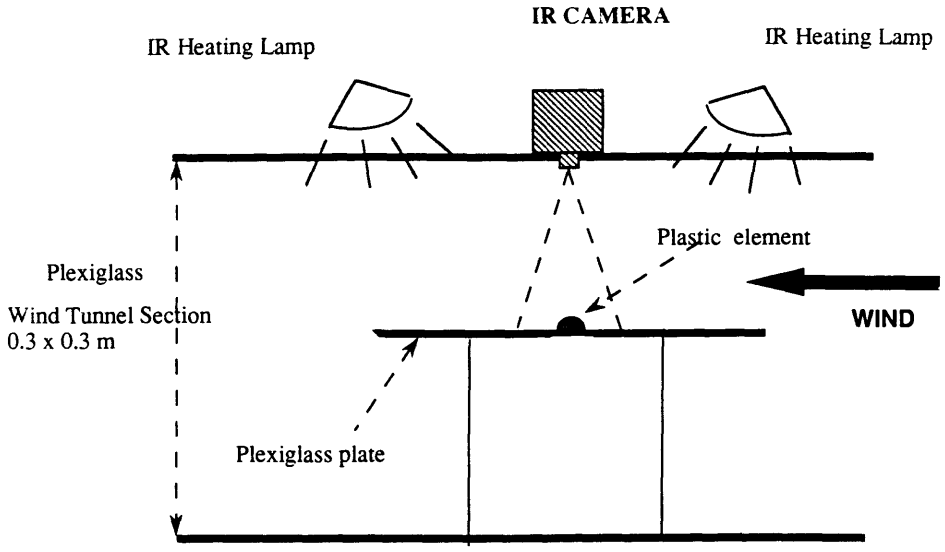

Figure 3-3: Schematic drawing of the dry wind tunnel tests set-up

Roughness Height	Base Diameter
0.75 mm	2.25 mm
2.80 mm	6.00 mm
0.70 mm	3.10 mm
1.70 mm	4.00 mm

Table 3.1: Dimensions of the four roughness elements tested

3.3 Test Matrix

Four individual roughness element sizes were tested with the thermographic technique presented in the previous section. The roughness elements consisted of spherical section. The size and shape of these elements were chosen to represent observed ice roughness during ice accretion tests. The four roughness elements were glued side by side on the plate, in the field of view of the infrared camera (figure 3-5), and were tested simultaneously. The dimensions of the roughness elements tested are listed in table 3.1.

Two sets of tests were performed. The first set was performed with a laminar

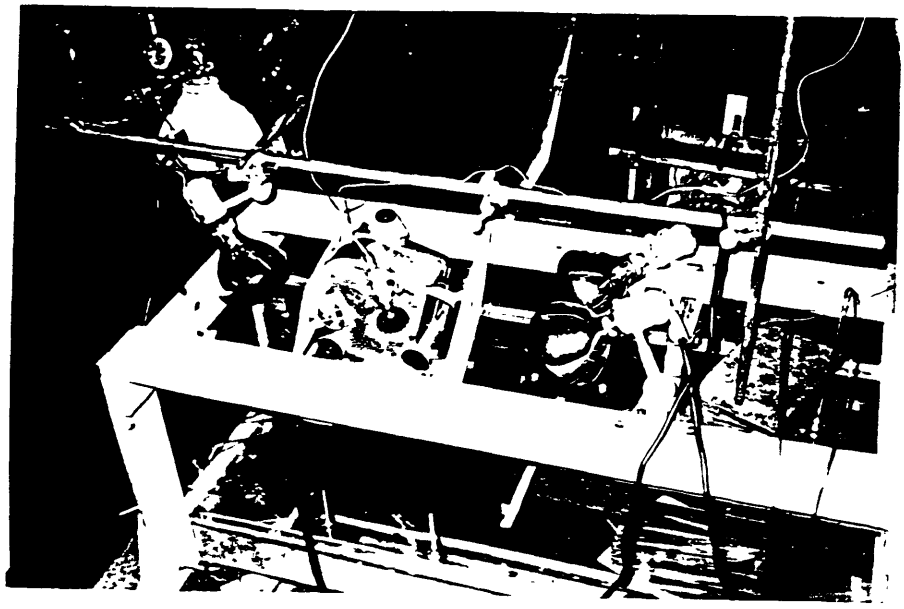

Figure 3-4: Picture of the actual set-up

boundary layer. Then, for the second set of tests, the boundary layer was tripped to turbulent, at the leading edge.

The range of airspeed tested was 4.5 m/s to 31.3 m/s, which, for the roughness configuration on the plate, corresponded to Reynolds numbers, based on the roughness location (Re_x), in the range of 70,000 to 450,000.

3.4 Results

The readings from the infrared camera were in good correlation with the thermocouple temperature readings. Discrepancies of less than 2° F were observed.

Figures 3-6 and 3-7 show typical thermographs of the 2.8 mm roughness element at 18 m/s, in the laminar and turbulent test cases, respectively. These pictures were taken in steady-state conditions. In all the tests, the lowest temperature, i.e. the highest convective heat transfer coefficient, was found at about 1/4 roughness diameter from the leading edge. Behind the roughness, a wake developed creating an area of enhanced heat transfer. Slightly upstream of the roughness, a decrease in the surface temperature was observed, both in laminar and turbulent tests, indicating

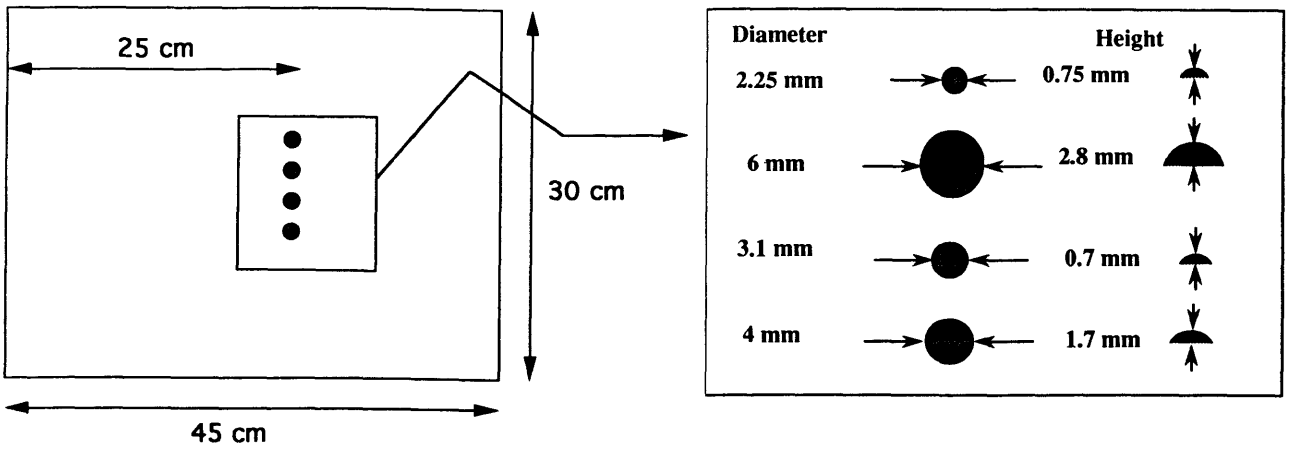

Figure 3-5: Flat plate and roughness elements dimensions

enhanced heat transfer upstream of the roughness.

3.4.1 Turbulent Heat Transfer Coefficient

The increase in the turbulent heat transfer coefficient, relative to the unperturbed region, is presented in figures 3-8 - 3-11, for the four different roughness elements,.

The peak of the heat transfer values were located at about 1/4 diameter of the roughness leading edge. This position is clearly shown in figure 3-9, where the larger element size allowed for more resolution. The observed increase in the relative convective heat transfer coefficient was of the order of 150% for the small elements, and of 240%, for the largest, and were found to grow slowly with Reynolds number (only about 10-15% over the range of Reynolds number tested). An exception to this was the largest element, as shown in figure 3-12.

3.4.2 Laminar Heat Transfer Coefficient

The increase in maximum heat transfer coefficient, relative to the unperturbed region, is presented, for the laminar tests, in figure 3-13 as a function of the local Reynolds

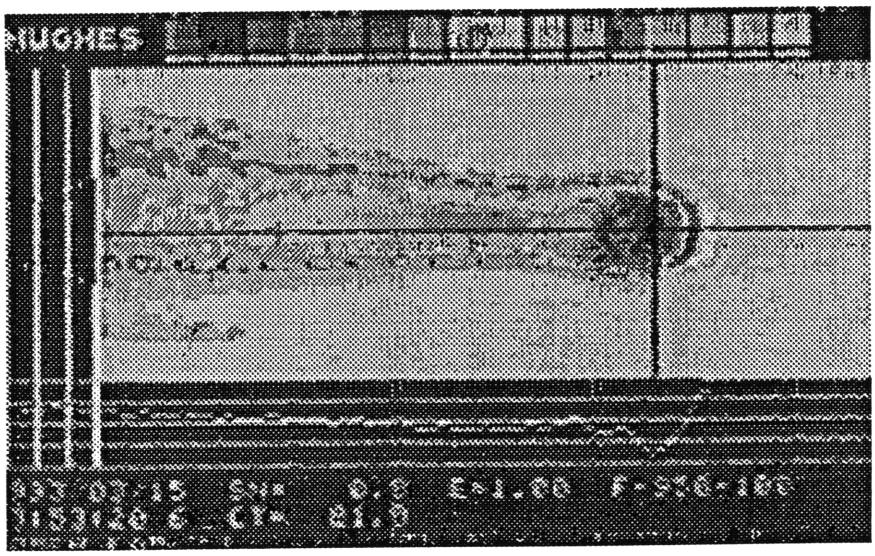

Figure 3-6: Typical thermograph of a heated roughness in the laminar cases

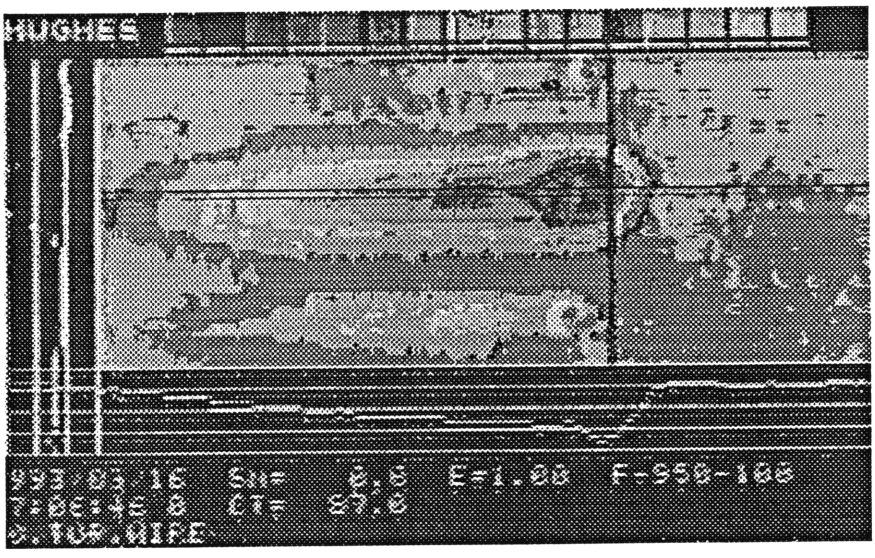

Figure 3-7: Typical thermograph of a heated roughness in the turbulent cases

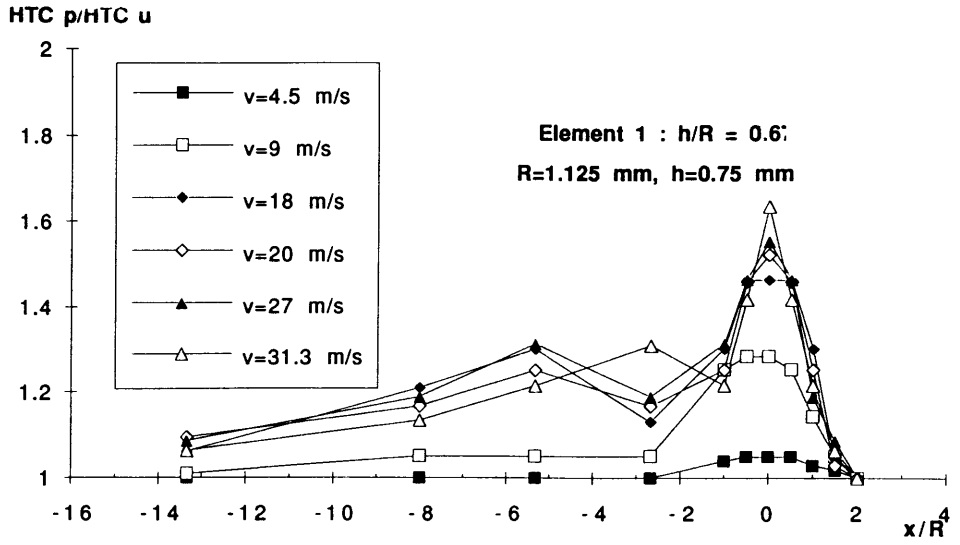

Figure 3-8: Relative increase in HTC for the 0.75 mm element; turbulent tests

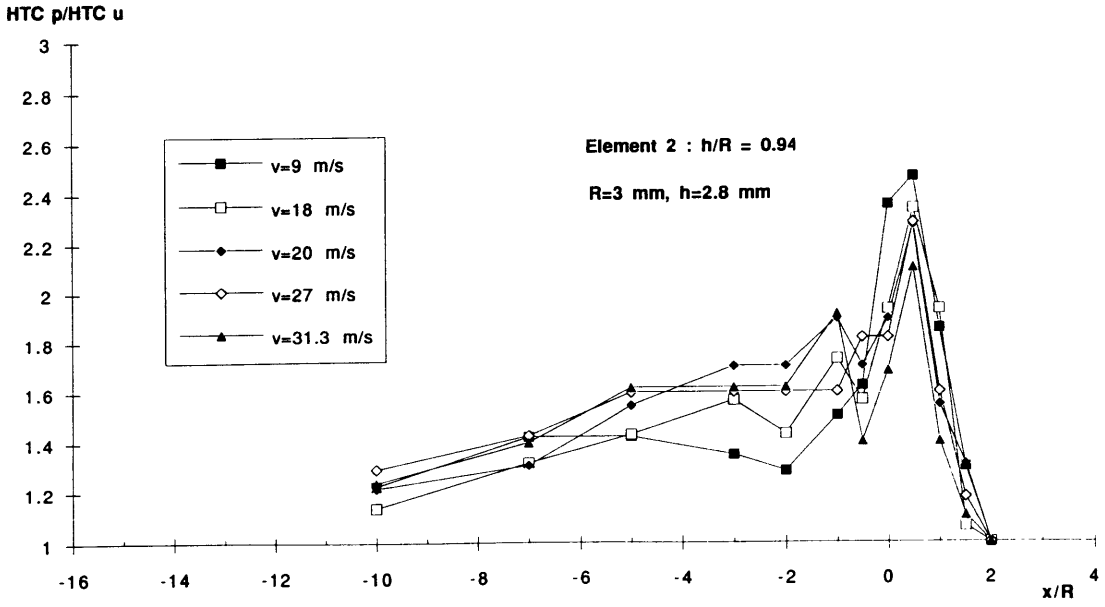

Figure 3-9: Relative increase in HTC for the 2.8 mm element; turbulent tests

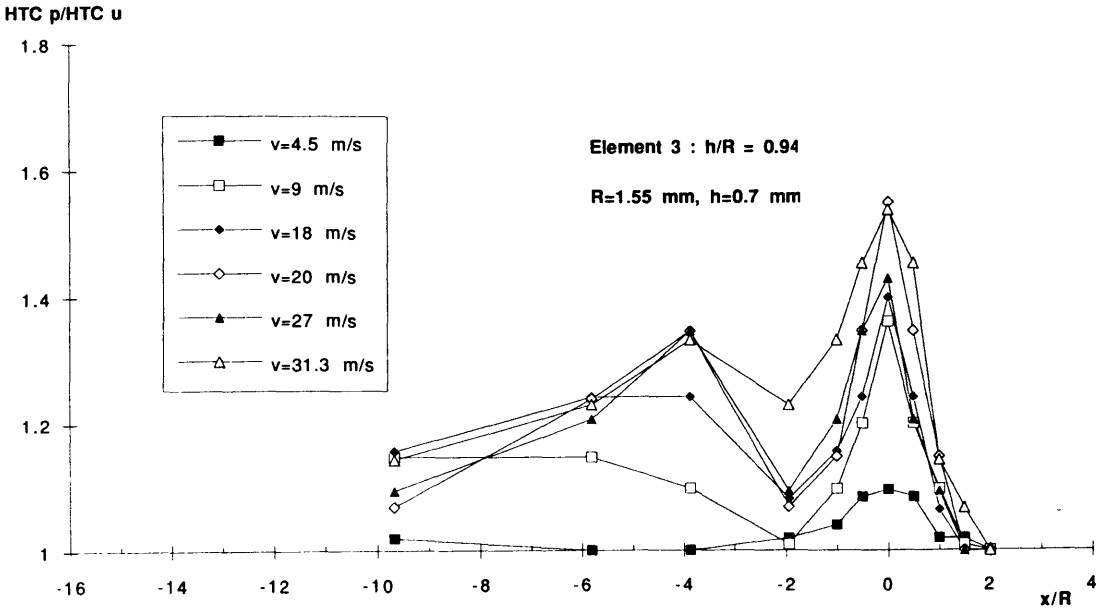

Figure 3-10: Relative increase in HTC for the 0.7 mm element; turbulent tests

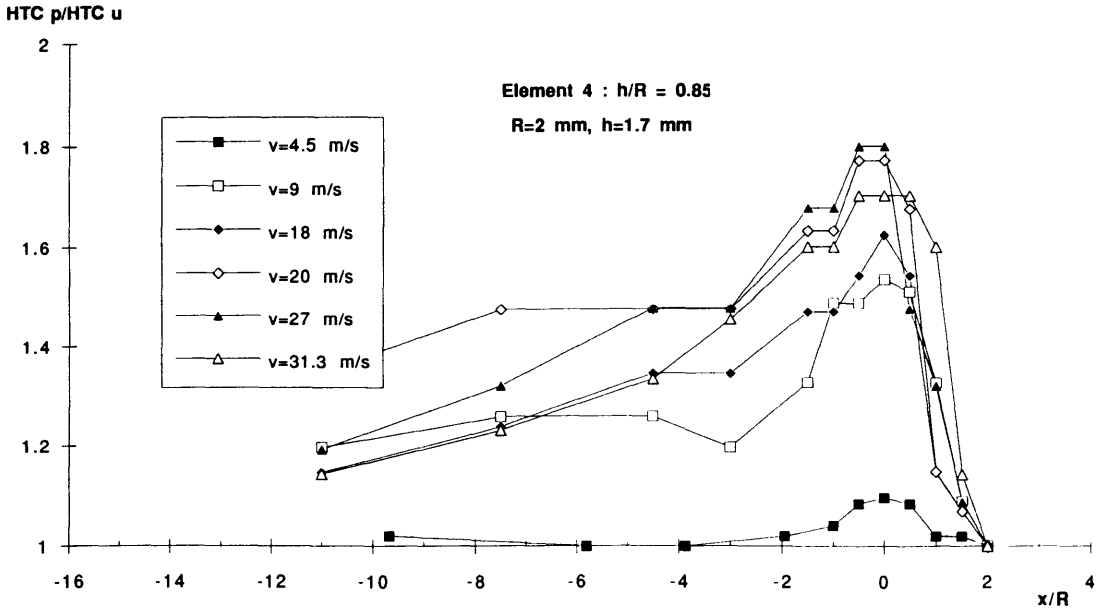

Figure 3-11: Relative increase in HTC for the 1.7 mm element; turbulent tests

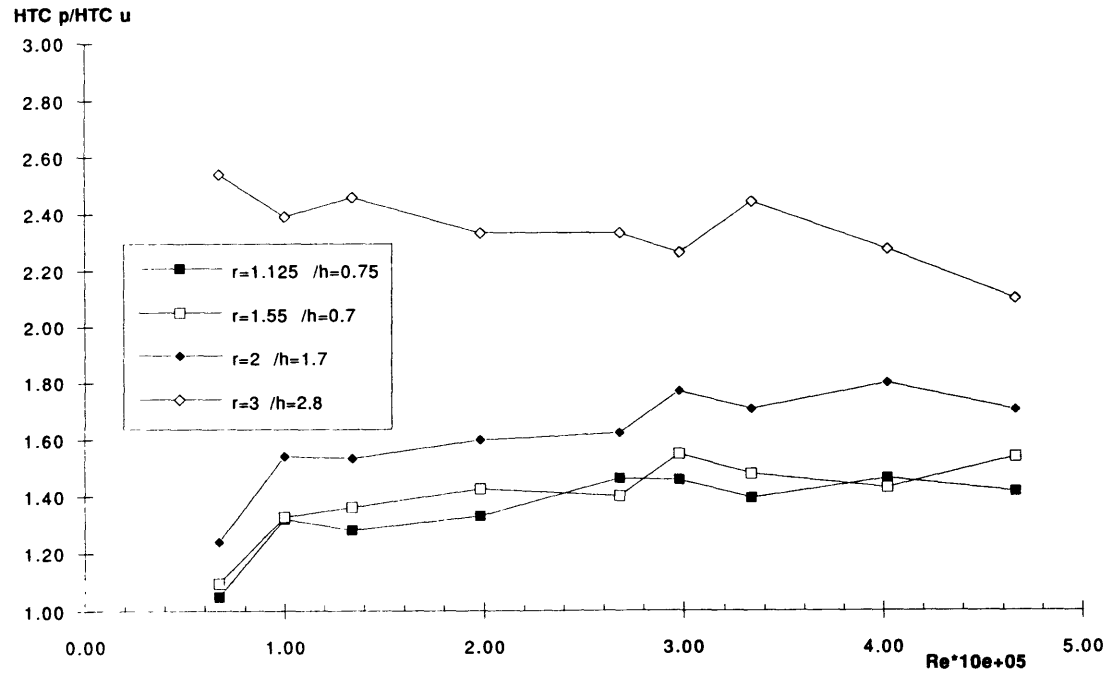

Figure 3-12: Relative maximum turbulent increase in HTC against Re_x

number Re_x.

In the laminar case, the maximum increase was also found on the frontal part of the roughness elements, at about 1/4 diameter. The maximum increase for the larger test elements (2.8 mm and 1.7 mm) were much larger in the laminar case than in the turbulent one. For the largest roughness element, a maximum heat transfer coefficient of 8 times the unperturbed value, was measured. For the 1.7 mm roughness, the increased heat transfer coefficient reached a maximum of 4 times the unperturbed heat transfer coefficient. For the smaller elements, the heat transfer coefficient did not even double. In these small roughness elements, i.e. 0.7-0.75 mm, the increase in convective heat transfer remained relatively low and constant, over the range of airspeed tested. It was also noted that, for the 2.8 mm and 1.7 mm roughness elements, the increase in HTC suddenly started dropping back, beginning from the 22.4 m/s test. This is thought to be due to the fact that the boundary layer was in fact turbulent for test speeds above 20 m/s.

To further understand the phenomenon, the increase in maximum relative heat transfer coefficient is plotted in figure 3-14 against the roughness element height nor-

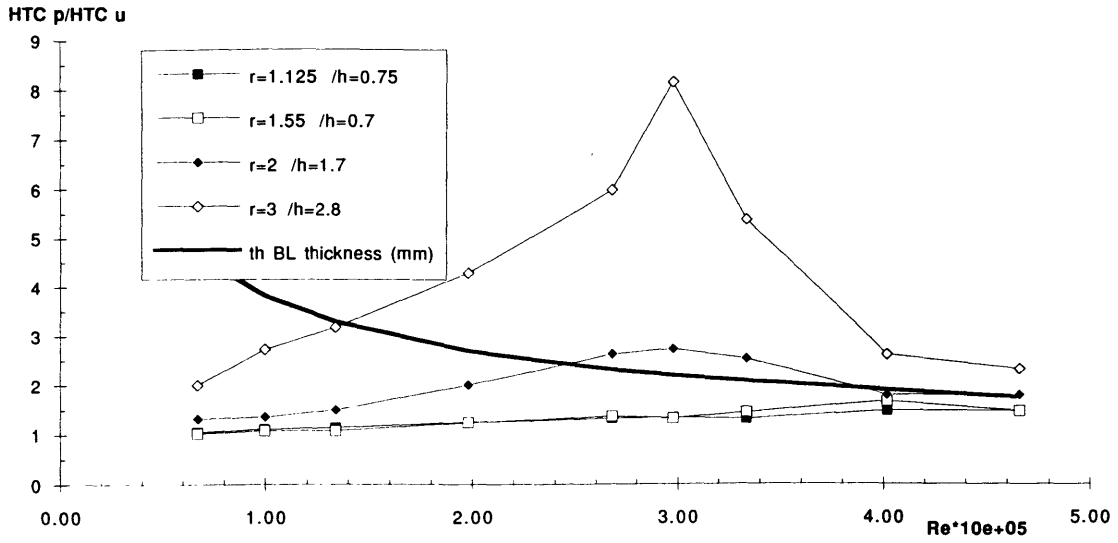

Figure 3-13: Relative maximum increase in laminar HTC against Re_x

malized by the boundary layer thickness. For large roughness elements, the convective heat transfer coefficient was strongly affected, up to the point where the boundary layer begun to transition to turbulence. At this point, the relative increase diminished in value and settled back in the 200% range. It must be pointed out that the increase was measured relative to an upstream value of the heat transfer coefficient, and hence, in the turbulent cases, the increase was relative to a turbulent convective heat transfer coefficient.

3.4.3 Additional Features

Two additional phenomena were noticed during the tests:

The Wake Behind the Roughness Element

The increase in heat transfer was transported by convection for a substantial distance behind the roughness element, as shown in the video prints in figures 3-6 and 3-7. The distance along which the disturbance was convected was over ten roughness element radii. This is clearly visible in figures 3-8 to 3-11. In some cases the wake of each

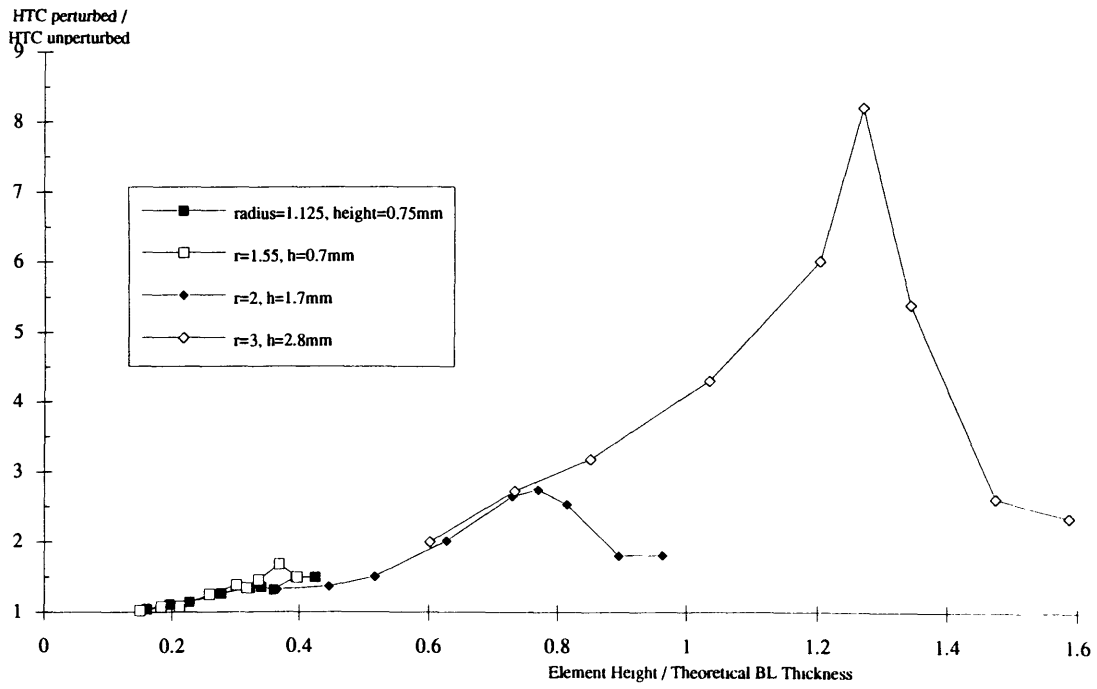

Figure 3-14: Relative maximum increase in laminar HTC against the normalized roughness height

element interfered with each other, creating additional increase in the heat transfer coefficient in the wake.

Heat Transfer Increase Preceding the Roughness element

Enhancement of the heat transfer coefficient on a short upstream distance was noted in all the tests. This initial increase in the heat transfer coefficient extended about one roughness element radius upstream, both in the laminar and turbulent boundary layer tests.

3.5 Comparison of the Laminar and Turbulent Tests

The following is an attempt to explain some of the phenomena encountered both in the turbulent and laminar tests; figure 3-15 shows two typical laminar and turbulent boundary layer profiles. The laminar boundary layer thickness is thinner than the

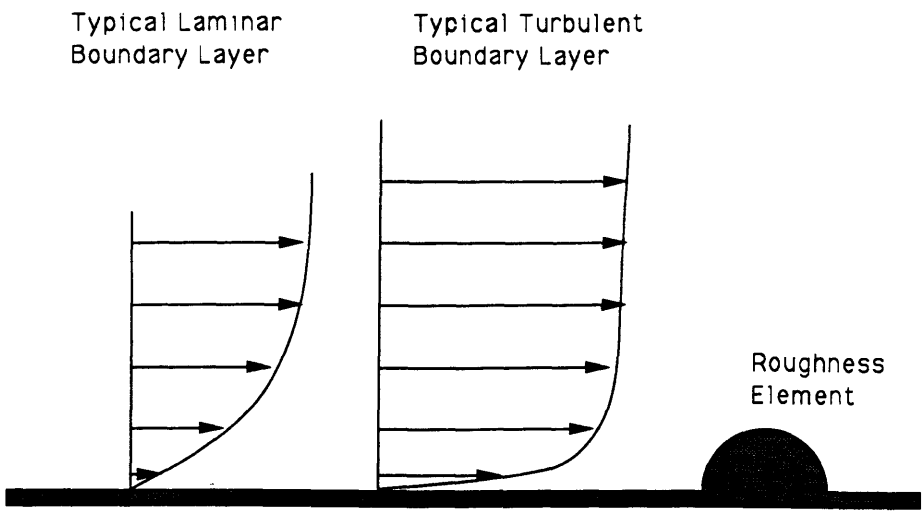

Figure 3-15: Typical laminar and turbulent boundary layer profiles

turbulent one, at a given Reynolds number. Yet the near-wall portion of the boundary layer profile where the flow is accelerated is much thinner in the turbulent boundary layer. Therefore, all the observed roughness elements in the turbulent boundary layer encountered a high airspeed, very close to the freestream velocity, independent of their size. In the laminar case, however, the flow accelerates less abruptly from the wall, and therefore the acceleration of the flow on the roughness is also due to this thicker shear layer. This is why, a variety of increases in relative HTC were found, for the laminar boundary layer cases. This is schematically represented in figure 3-15.

3.6 Implications for Ice Accretion Models

Most of the accreting surfaces on an airfoil have a turbulent boundary layer, once some ice roughness has grown. Hence, the observations and analysis of the phenomenon occurring in the turbulent tests are the most interesting ones. In this experiment, it was found that the *tip of a feather* experienced a turbulent convective heat transfer coefficient as high as two and a half the turbulent one that is present at its base. This quantitative data is of primary importance since this increased convective heat transfer coefficient will influence the determination of the feather growth regions and govern the rate of growth of the feathers.

It was also found that the heat transfer coefficient was already increased in front of

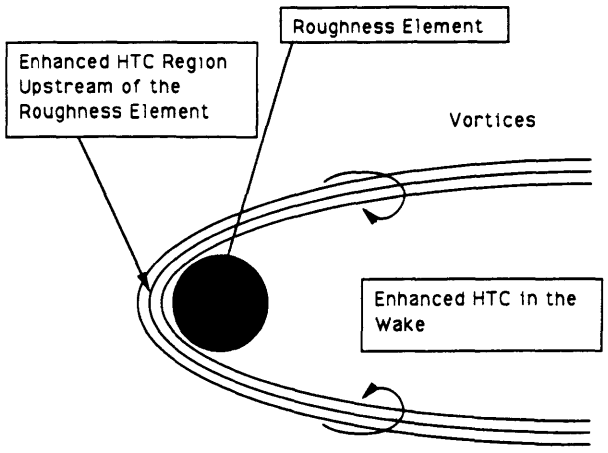

Figure 3-16: Schematic representation of the vorticity developing around a roughness element

the roughness element. This observation, if quantified, could help build a model that simulates the first instants of ice accretion, where the roughness progresses towards the stagnation line, as already reported in chapter 2 and schematically represented in figure 2-28. Figure 3-16 shows schematically how the author and his collaborators interpret the phenomenon; vorticity develops around the roughness element, causing higher convection of the surface heat, or, in the case of ice accretion, of the latent heat of freezing.

The roughness model included in Lewice uses the *equivalent sand grain* technique that Schlichting [25] developed based on Nikuradse's experiments. The concept of equivalent sand grain roughness height was introduced as a means of characterizing other types of roughness elements by referring to the equivalent net effect produced by Nikuradse's experiments. Consequently, this technique considers the roughness as a global and homogeneous parameter, and computes an *averaged* heat transfer coefficient.

In the case of feathers, the effect was *local.* The equivalent sand grain theory is not be able to model local increase in heat transfer on the tip of roughness element, and will, therefore, not predict the observed rime in mixed ice conditions. A more effective heat transfer prediction model should have the ability to provide for, at least, two heat transfer coefficients in a rough zone: one for the peak of the roughness elements, and one for their base.

Chapter 4

Improved Ice Growth Model

4.1 Summary of the Observed Physics

Based on the analysis of the close-up video recordings, several phenomena were identified which strongly influenced the ice growth. Dominant amongst these was the presence of feather growth in most accretion regions of rime and mixed ice accretions. In the dry wind tunnel tests, quantitative data, for the local heat transfer increase on small roughness elements, were obtained.

The following is a listing of the observed physics that are not commonly implemented in current ice accretion models:

- Feather growth in the direction of impingement: impinging droplets were observed to freeze on impact and accrete in the form of feather, which grew in the direction of impingement.

- The filling of interstitial gaps: feathers can be considered as units of rime growth. They grow on individual sites, and therefore have considerable gaps in between (figure 2-12 - 2-16). Wet growth was observed in these gaps, and therefore, the density of rime accretions is changed during the accretion process.

- Local heat transfer enhancement: in the dry wind tunnel tests, small roughness elements have experienced an increased convective heat transfer coefficient, close

to their tip. Dry and wet growths can occur on a single numerical cell, if feathers have developed.

- Limits of feather growth regions: the feathers grew only were the value of the local heat transfer was high enough. These feather growth limits were observed to change as runback water filled the interstitial gaps.

4.2 Description of the Model

It is impractical to model each individual feather in the feather growth region. The ice growth model presented here, uses a simple *bulk* approach for the feather growth regions. When rime ice is predicted, the height of the feathers will be represented as a bulk mass of rime ice. The individuality of the feather growth is kept through the possibility of filling in the interstitial gaps with runback water and glaze ice. Glaze ice accretion is allowed to occur inside the bulk rime feathers, within the interstitial gaps.

The difficulty remains in determining where feather growth occurs. The limit of the feather growth regions was observed to move away from the stagnation region in the mixed ice accretion cases, as the interstitial gaps were filled.

In order to model feather growth, several changes must be implemented in the current ice growth models:

- The ice growth modeling should be altered to allow for two growths:

    1. Growth in the direction of impingement, within the predicted feather growth limits.
    2. Growth normal to the surface, for the predicted glaze ice accretion regions, in mixed and glaze ice accretions.

- Modifications to the mass and energy balances must be made to separate feather growth from wet ice growth, within the same numerical cell.

- Modifications to the ice density routine should be implemented to accommodate the filling, with glaze ice, of the interstitial gaps inside the rime feathers bulk.

The following three paragraphs will describe each of the previously mentioned modifications, and recall the models used in Lewice.

4.2.1 Ice Growth Calculation

In the icing tests presented in chapter 2, impinging water was observed to accrete on impact and form feathers. The feathers then grew in the impact direction of the instantly freezing droplets.

In contrast to this, the runback water, freezing under low freezing fraction as it runs along the iced surface, grows is in the direction normal to the glaze surface.

Lewice Ice Growth Approach

Most ice accretion prediction codes, including Lewice, accrete the total amount of water frozen ($\dot{m}_{ice}$) normal to the surface, everywhere on the body. The actual computation performed in Lewice for the ice growth is presented in equation 4.1.

$$dh = \frac{\dot{m}_{ice}}{\rho \, ds} \tag{4.1}$$

Improved Ice Growth Approach

The new model incorporates both growth directions. Following the local freezing fractions (equations 4.4 and 4.5), one or both of the growth modes is chosen. If rime growth occurs, then ice growth is in the direction of impingement. If runback water freezes, it will be accreted normal to the glaze surface.

4.2.2 Dual Surface Growth

In most mass balance models used to calculate the local freezing fraction in ice accretion simulation codes, the mass of impinging water is added to that of the unfrozen

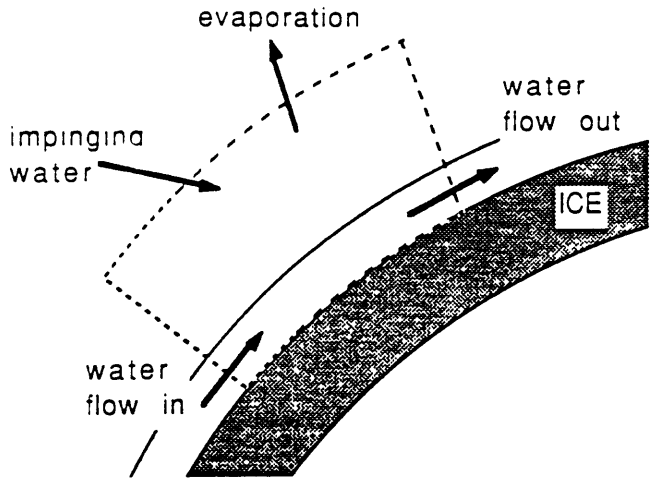

Figure 4-1: Schematic drawing showing the control volume and masses used in Lewice mass balance [20]

water running back, to calculate the total mass of incoming water. The local freezing fractions are subsequently computed, and the nature (i.e. dry or wet) of the ice determined, following existing empirical models. Glaze ice accretion is the only case where, adding the impinging mass of water to the runback water, is the correct course of action. Since one cannot know a priori what is the type of ice that will form, the freezing fraction on the impinging mass of water must first be calculated.

Lewice Mass Balance Approach

In Lewice, the mass balance used to calculate the local freezing fraction adds the impinging water mass flux ($\dot{m}_{imp}$) to the runback water mass flux ($\dot{m}_{run_{in}}$). Evaporation of water is accounted for in Lewice model, and expressed by $\dot{m}_{evap}$. The actual mass balance, extracted from Lewice's User's Guide [21], is expressed in equation 4.2, and described in figure 4-1:

$$\dot{m}_{imp} + \dot{m}_{run_{in}} - \dot{m}_{evap} - \dot{m}_{run_{out}} = \dot{m}_{ice} \tag{4.2}$$

The freezing fraction (η) is then calculated for the local control volume defined in figure 4-1, as the ratio of added ice mass ($\dot{m}_{ice}$) the added water mass, as in

equation 4.3:

$$\eta = \frac{\dot{m}_{ice}}{\dot{m}_{run_{in}} + \dot{m}_{imp}} \tag{4.3}$$

The added water mass is the sum of the impinging and runback water masses. This model uses a single mass balance equation, and does not distinguish between glaze and rime growth mechanisms.

Feather Growth Surface

The proposed physical model allows for the growth of rime feathers, as well as for the growth of glaze ice. Feathers were observed to grow individually on existing small ice roughness. The feathers are fed by the impinging water alone, at their tip. Because feathers are high above the substrate, they are not in contact with the runback water, and therefore they can grow even when water runback is predicted.

The modeling of rime feathers requires a separate local mass balance on the impinging water droplet mass, followed by a separate freezing fraction calculation, on a single numerical cell. The computation of the feather freezing fraction η_{imp}, as expressed in equation 4.4 is used to check the possibility of rime feathers accretion. In equation 4.4, $\dot{m}_{feather,h_{enhanced}}$ refers to the mass flux of rime ice (i.e. feathers) added. The use of an enhanced local convective heat transfer coefficient value for the feather growth, should permit to grow rime feathers even on relatively wet surfaces, as observed in many tests. An enhancement of about 250% is recommended, based on the turbulent convective heat transfer coefficient measurements performed in the infrared thermography tests. In the cases where the feather tip freezing fraction is less than unity, feather growth is not predicted and glaze ice is accreted, after adding the impinging mass to the runback water, as in the standard model used in Lewice.

$$\eta_{imp} = \frac{\dot{m}_{feather,h_{enhanced}}}{\dot{m}_{imp}} \tag{4.4}$$

Glaze Growth Surface

In the cases where the local freezing fraction of the iced surface reaches unity, and water droplets impinge on it, feather growth will be confirmed. If water is running into the zone where these feathers were predicted, a second freezing fraction should be calculated and glaze ice grown. Equation 4.5 is used to compute the freezing fraction of the running water, using the normal convective heat transfer coefficient in the energy balance.

$$\eta_{runback} = \frac{\dot{m}_{glaze,h_{normal}}}{\dot{m}_{run_{in}}} \tag{4.5}$$

In equation 4.5, $\dot{m}_{glaze,h_{normal}}$ stands for the glaze ice mass flux. Thus, in this model, the mass of the impinging water can be separated from the runback water, if the impinging water's freezing fraction is unity. We now have two separate accreting surfaces, with different convective heat transfer coefficients. But the glaze ice surface accretes where rime ice already exists, at a lower density. The following section shows how the improved model, negotiates this difficulty and actually adds more physics to the previous model.

4.2.3 Ice Density Calculation

The model first checks if, within the impingement limits, feathers can grow. This is achieved by checking if the freezing fraction, based on the impinging mass of water alone, and the enhanced heat transfer coefficient, reaches unity. If water runs inside the impingement limits, where feathers were predicted, glaze ice will form in the interstitial gaps.

Lewice Ice Density Approach

In Lewice, as in most ice accretion prediction codes, the ice density is determined by using empirical formulas. The most widely used relation is the Macklin correlation [14] (equation 4.6) that uses three parameters: the mass median droplet diameter $\bar{d}_m$ in microns, the droplet impact velocity V_d in m/sec, and the surface temperature

T_{surf} in °C.

$$\rho = 110 \ (\frac{\bar{d}_m \ V_d}{2 \ |T_{surf}|})^{.76} \tag{4.6}$$

Macklin correlation is used only when the following two conditions are fulfilled:

$$1 \frac{\mu m \ m}{sec \ ^oC} \ \leq \ \frac{\bar{d}_m \ V_d}{2 \ |T_{surf}|} \ \leq \ 17 \frac{\mu m \ m}{sec \ ^oC} \tag{4.7}$$

$$T_{surf} \ < \ -5^oC \tag{4.8}$$

In other conditions, the ice is assumed to be glaze and to have a density of 917 kg/m^3.

Recently another empirical model has been proposed, and implemented in a newer version of Lewice. This model [27] determines the ice density using five parameters, rather than three in the Macklin model.

Once the density of the ice is calculated, it cannot be altered by the surface runback water that might subsequently find its way across the accretion. Observations have proved that rime ice can be filled in with water, and take the form of mixed ice. This limitation in Lewice can be overcome by implementing the following density model.

Improved Ice Density Approach

In the new model, feathers are first grown wherever possible. The density of the feathers is determined with the use of any of the known empirical correlations. Then, runback water is allowed to flow, starting from the stagnation point. The surplus water finds its place where the local thermodynamics enables it to freeze, following the second freezing fraction calculation $\eta_{runback}$. There, it freezes, filling the gaps within the feathers, rising the value of the rime density to the glaze ice density.

The thickness of this interstitial glaze ice filling can be determined with the following equation:

$$dh_{fill} \ = \ \frac{m_{run_{in}} \ \eta_{runback}}{(\rho_{glaze} - \rho_{feather}) \ ds} \tag{4.9}$$

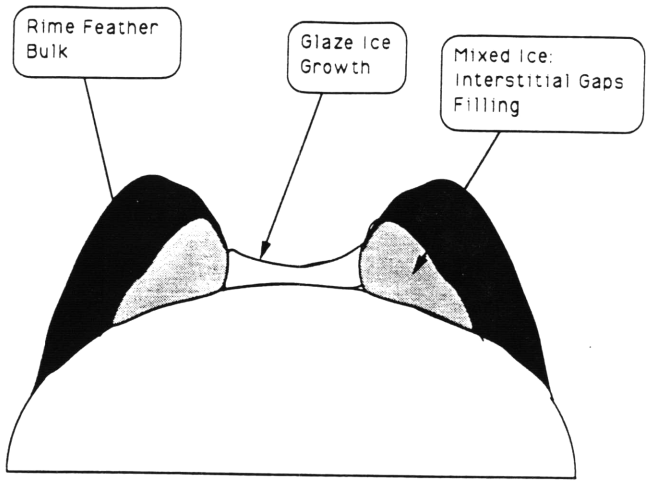

Figure 4-2: Schematic drawing showing the rime and glaze accreting surfaces

The glaze ice now fills the feathers up to the height calculated in equation 4.9, and this density, which is the highest accreting ice can achieve, is definitive. This is represented schematically in figure 4-2. The feathers are first formed, then the runback water freezes and fills in the lower density of the feathers.

Note that in reality, feathers and the glaze ice beneath grow simultaneously. The new model being presented here separates the two phenomena.

4.3 Discussion of the Improved Model

Some problems can occur in the frame of the new ice growth model. For instance, what happens if the thickness of the glaze ice accretion under the tip of a rime accretion, exceeds the thickness of the rime ice bulk ? In order to answer this question, we need to refer to the icing tests, and the close-up observations. In certain cases, the freezing fraction on the tip of a feather was high enough to produce rime ice. Yet, later on in the same test, the rime feather growth had stopped. Prior to that event, runback water was filling in the interstitial gaps. When the feather growth stopped, the water began flowing over the feather tips. It is very tempting to conclude that the excess of runback water actually caused the freezing fraction on the tip of the feather

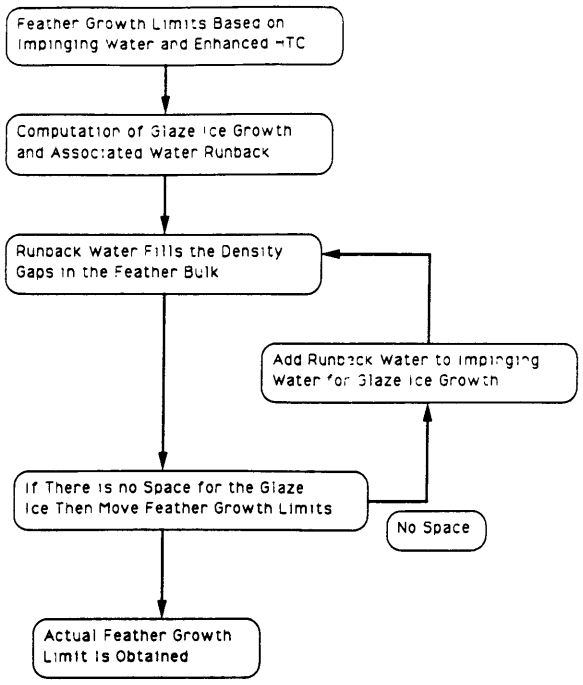

Figure 4-3: Algorithm for the determination of local feather growth

to suddenly become lower than unity. Consequently the impinging water began to freeze as glaze ice, together with the local runback water. It appears that the feather growth previously observed, mutated to a normal to the surface glaze growth, where both impinging and runback water are blended together as in the older model. This would explain the Type A horn growth stop observed and reported in chapter 2.

4.3.1 Determination of the Feather Growth Limits

A complete ice growth model has now taken shape. The total model iteratively checks the presence of feathers within the impingement limits. Figure 4-3 shows the algorithm of the model's iteration on feather growth search.

First the local freezing fraction, η_{imp} in equation 4.4, is checked on top of the rime surface, within the impingement limits. The convective heat transfer coefficient is enhanced using characteristic values found in the dry tests, presented in chapter 3. The limits of the possible feather growth are set, as shown in figure 4-4. The mass

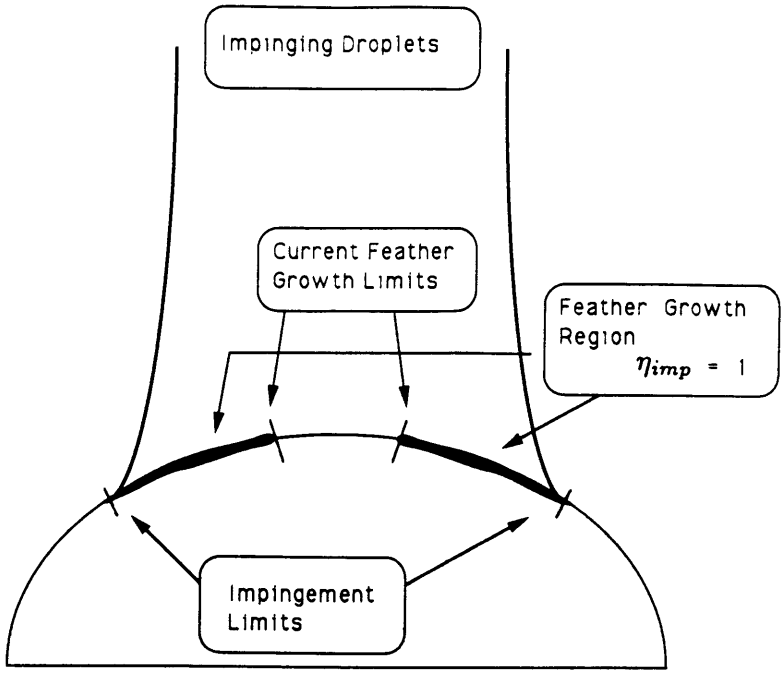

Figure 4-4: Impingement limits and feather growth limits

and energy balances were calculated, using only the impinging water droplet masses. The rime feather bulk is grown in the local direction of impingement. As discussed earlier, the feather growth possibility is not really yet, definitive: the mass and energy balances on the runback water have yet to be computed. A different local freezing fraction ($\eta_{runback}$ in equation 4.5) is computed, using only the runback water flux resulting for the unfrozen impinging water. The runback water is grown in a normal to the surface direction, while its thickness is computed using equation 4.9. This was presented in figure 4-2. It is now possible possibility to check if feather growth occurs, specially in the neighborhood of the inner feather growth limits, close to the stagnation line. Whenever the predicted feather growth is rejected, the runback and impinging water are added and frozen normal to the surface, with the excess water continuing the water runback process. The feather growth limits are then moved backwards, towards the impingement limits, as shown in figure 4-5.

This model shows more understanding of the ice growth physical process, but rely on the accurate prediction of the convective heat transfer coefficient. The convective

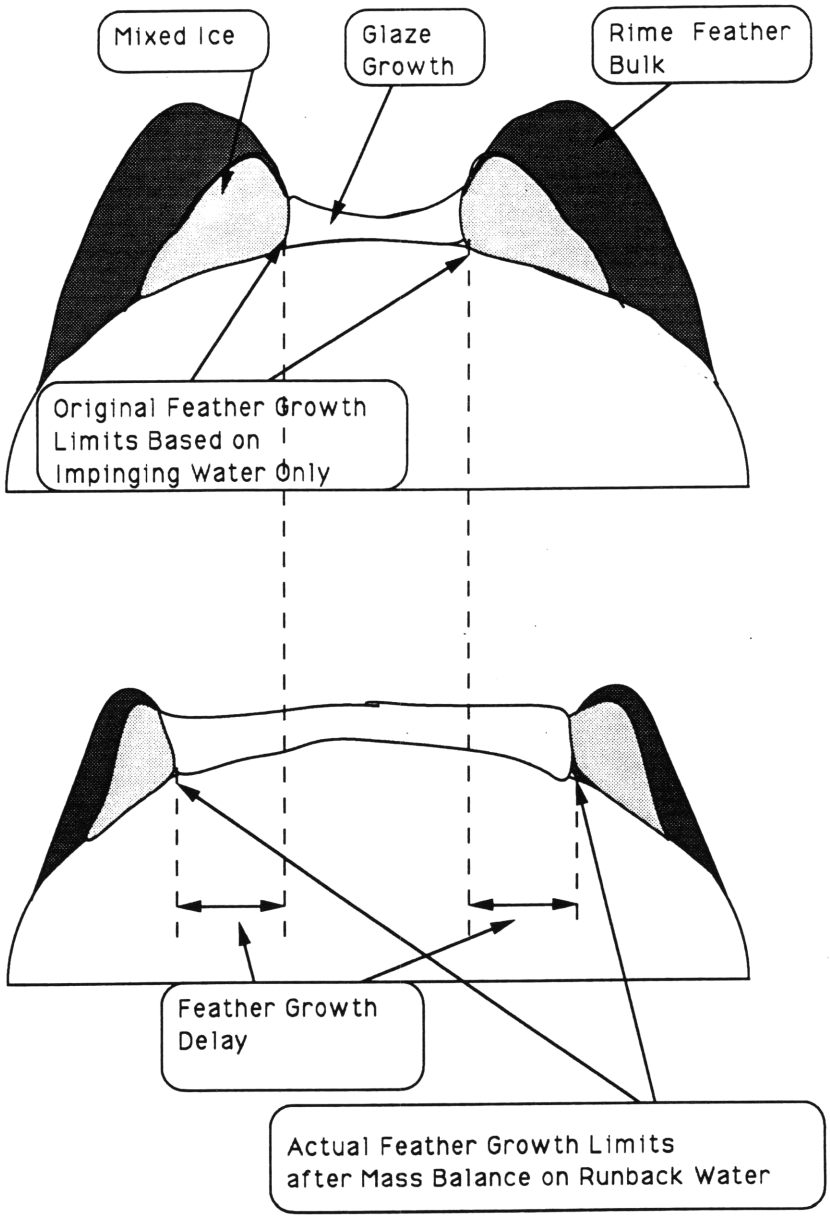

Figure 4-5: Runback water delays feather growth by overflowing the rime accretion

heat transfer coefficient is a strong function of the local ice roughness height. The measurement of the roughness height is however, beyond the scope of this work. More empirical data of ice roughness would be needed to complete this model, and faithfully model real ice accretion.

Chapter 5

Conclusions

5.1 Summary of Observations

The icing wind tunnel tests and the dry heat transfer tests have resulted in the following observations:

Feather Formation

- In rime and mixed ice accretion regimes, feather growth was observed. These feathers grew in an inverted conical shape, in the local impingement direction.
- Feathers were observed to have grown out of an initial ice roughness element.
- The feathers were observed to be formed by impinging droplets freezing at their tip, where the heat transfer was high.
- Due to their inherent formation mechanism, interstitial gaps developed at the feathers' root. The number of feathers per unit area was low in mixed ice accretion regimes or when initial roughness was present. In rime accretion regimes or on initially smooth surfaces, the number of feathers per unit area was higher.
- Feather growth rates have been measured. Feathers exhibited a slow start followed by a faster steady-state growth which was found to be proportional to

the total water mass flux ($LWC\ V$).

Rime Ice Accretion

- In rime ice accretions, feathers were observed to form inside the impingement region.
- In very cold rime accretions, shedding of part or whole feathers was observed, which contributed to the typical aerodynamic shape of rime accretions.

Mixed Ice Accretion

- In mixed ice accretion regimes, large feathers formed at the impingement limits where the heat transfer was high.
- In the stagnation region of mixed ice accretions, where the heat transfer coefficient was low, excess water ran back.
- In mixed ice accretions, runback water from the stagnation region froze in the interstitial gaps of the feathers forming at the impingement limits.

Glaze Ice Accretion

- In glaze ice accretion regimes, where the freezing fraction did not reach unity, excess water was observed to run back in the form of film or rivulets.
- This runback water froze downstream and formed glaze ice. The glaze ice was observed to grow normal to the iced surface.

Horn Formation

1. Type A Horn
    - In mixed ice accretions, Type A horns were observed. These mixed horns grew in the direction of the flow, at the interface between dry and wet growths.

- In some cases, Type A horn growth was stopped by excessive runback water that covered the accreting tip of the feathers.

2. Type B Horn

   - In glaze ice accretions, Type B horns were observed. These glaze horns grew at the limit of accretion, where large ice roughness had developed. Due to their growth normal to the surface, Type B horns spread outwards.
   - Type B horns were observed to grow further downstream as the median volume diameter of the impinging droplets was increased.

Increase in Convective Heat Transfer on Small Roughness Elements

- Both in turbulent and laminar boundary layers, the heat transfer coefficient on a small roughness element was observed to increase at the leading edge.
- In all the tests, the maximum heat transfer coefficient was observed at the same position, 1/4 diameter downstream from the leading edge.
- In the laminar boundary layer cases, the maximum HTC increase varied between about 150% and 800% depending upon the element size; higher elements having higher heat transfer coefficient increase.
- In the turbulent boundary layer cases, the maximum HTC increase varied between about 150% and 240% depending upon the element size; higher elements having higher heat transfer coefficient increase.
- Increase of the heat transfer coefficient was also noted slightly upstream of the element, in both boundary layer regimes. This phenomenon is thought to influence the progression of the rough region in the first instants of glaze and mixed ice accretions.
- A wake developed behind the roughness element where the increase in the heat transfer was maintained for a distance of more than 10 roughness element radii.

5.2 Features of Improved Ice Growth Model

Most of the physical phenomena identified in the analysis of the experiments performed in the scope of this thesis have been implemented in an improved ice growth model. The features of the resulting accretion model are listed herewith:

- Growth in the direction of the impinging droplets is allowed in the feather growth region. This growth is applied to the mass of impinging droplets only.
- An enhanced convective heat transfer coefficient is considered for the feather growth. The enhanced heat transfer coefficient is computed by increasing the predicted heat transfer on the glaze surface, by a factor of about 2.5, as observed in the turbulent dry infrared tests.
- A bulk rime growth approach is proposed as a practical method to accrete feathers. This growth involves only impinging droplets and is based on the enhanced heat transfer coefficients.
- This model enables glaze ice formation inside the bulk of rime ice, to reproduce the observed filling of the interstitial gaps. This is performed by maintaining two growth surfaces: the surface of the bulk feather growth and the surface of the wet growth, underneath the rime bulk.

Bibliography

[1] P. Perkins and W. Rieke. Aircraft Icing Problems - After 50 Years. *AIAA 93-0392*, 1993.

[2] Ohio Aerospace Institute. Aircraft Icing. Short Course Notes, September 1992.

[3] A.L. Reehorst. Users' Guide to Twin Otter for Natural Icing Research. NASA publication - distributed by the Icing and Cryogenics Technology Branch.

[4] D. Belte and R. Woratschek. Helicopter Icing Spray System (HISS) Evaluation and Improvements. Technical Report Project No. 82-05-3, USAAEFA, 1986.

[5] W. Olsen. Survey of Aircraft Icing Simulation Test Facilities in North America. *NASA TM 81707*, 1981.

[6] Francois Charpin and Guy Fasso. Icing Testing in the Large Modane Wind Tunnel on Full Scale and Reduced Scale Models. *NASA TM 75373*, 1972. English Translation.

[7] Robert Henry and Didier Guffond. Infrared Technique to Measure the Skin Temperature on an Electrothermal Deicer - Comparison with Numerical Simulation. *AIAA-89-0760*, 1989.

[8] M.G. Potapczuk and J.J. Reinmann. Icing Simulation: A Survey of Computer Models and Facilities. *NASA TM 104366*, 1991.

[9] M.G. Potapzcuk and M.T. Velazquez. Ice Accretion and Performance Degradation Calculations with LEWICE/NS. *AIAA-93-0173*, 1993.

[10] B.L. Messinger. Equilibrium Temperature of an Unheated Icing Surface as a Function of Airspeed. *Journal of the Aeronautical Sciences*, Vol. 20:pp. 29–42, 1953.

[11] J.L. Hess and A.M.O. Smith. Calculation of Potential Flow about Arbitrary Bodies. *Progress in Aeronautical Sciences*, Vol. 8:pp. 1–138, 1967.

[12] Irving Langmuir and Katharine B. Blodgett. A Mathematical Investigation of Water Droplet Trajectories. Technical report, Army Air Force Technical Report No. 5418, February 1946.

[13] Tribus, Myron, Young, G.B.W., and Boelter, L.M.K. Analysis of Heat Transfer over a Small Cylinder in Icing Conditions on Mount Washington. *Trans ASME*, Vol. 70:pp.871–876, 1949.

[14] W.C. Macklin. The Density and Structure of Ice Formed by Accretion. *Quarterly Journal of the Royal Meteorological Society*, Vol. 88:pp. 30–50, 1962.

[15] R.J. Jr. Hansman and Turnock S.R. Investigation of Surface Water Behavior During Glaze Ice Accretion. *Journal of Aircraft*, 1989.

[16] Hansman, R.J. Jr, Yamagushi, K., Berkowitz, B., and Potapzcuk, M. Modeling of Surface Roughness Effects on Glaze Ice Accretion. *AIAA-89-0734*, 1989.

[17] W. Olsen and E. Walker. Experimental Evidence for Modifying the Current Physical Model for Ice Accretion on Aircraft Surfaces. *NASA TM 87184*, 1986.

[18] Hansman, R.J. Jr., Reehorst, Andrew, and Sims, James. Analysis of Surface Roughness Generation in Aircraft Ice Accretion. *AIAA-92-0298*, 1992.

[19] Hansman, R.J. Jr., Breuer, K.S., Hazan, D., Reehorst, A., and Vargas, M. Close-up Analysis of Aircraft Ice Accretion. *AIAA-93-0029*, 1993.

[20] Keiko Yamagushi. Improved Ice Accretion Prediction Techniques Based on Experimental Observations of Surface Roughness Effects on Heat Transfer. Master's thesis, Massachusetts Institute of Technology, May 1990.

[21] A. Gary Ruff and M. Brian Berkowitz. *Users Manual for the NASA Lewis Ice Accretion Prediction Code (LEWICE)*, 1990. NASA CR 185129.

[22] Ronald H. Soeder and Charles R. Andracchio. *NASA Lewis Icing Research Tunnel User Manual*, 1990. NASA TM 102319.

[23] Pascal Personne. *Effet de la rugosite sur la croissance du givre a faible vitesse: resultats experimentaux et modelisation.* PhD thesis, Universite Blaise Pascal, 1988.

[24] P. Personne and C. Duroure. Influence de la rugosite du givre sur sa croissance par la captation des gouttes d'eau surfondue: application au givrage des cables electriques. *Journal de Physique*, Vol. 48:pp. 389–395, 1987.

[25] H. Schlichting. *Boundary-Layer Theory.* McGraw-Hill, 7th edition edition, 1979.

[26] Yamagushi, K., Hansman, R.J. Jr., and Kazmierczak, M. Deterministic Multi-Zone Ice Accretion Modeling. *AIAA-91-0265*, 1991.

[27] M. Rios. Icing Simulations Using Jone's Density Formula for Acrreted Ice and Lewice. *AIAA-91-0556*, 1991.

[28] Frost, W., Chang, H., Shieh, C., and Kimble, K. Two-Dimensional Particle Trajectory Computer Program, 1982. Interim Report for Contract NAS3-22448.

[29] Robert Henry et al., 1994. AIAA Paper to be published.